Journal of Fluids and Structures 130 (2024) 104173

Contents lists available at ScienceDirect

Journal of Fluids and Structures

journal homepage: www.elsevier.com/locate/yjfls

Hydroelastic wave interaction with a circular crack of an ice-cover in a channel

Y.F. Yang, G.X. Wu *, K. Ren

Department of Mechanical Engineering, University College London, Torrington Place, London WC1E 7JE, UK

ARTICLE INFO

Keywords:
Ice sheet
Channel
Circular crack
Wave diffraction
Eigenfunction expansion
Green function method

ABSTRACT

Hydroelastic wave interaction with a circular crack of an ice-cover in a channel together with some related problems is considered, based on the linearized velocity potential theory and Kirchhoff plate theory. The domain decomposition method is adopted in the solution procedure. Two sub-domains are divided by the crack, one below the inner ice sheet and the other below the outer ice sheet. By using the Green function of an ice-covered channel, the velocity potential in the outer domain is established from the source distribution formula over an artificial vertical surface extended from the crack. The source distribution is expanded in both vertical and circumferential directions, which allows the velocity potential to be obtained in an explicit form with unknown coefficients. The velocity potential in the inner domain is expanded into a double series. An orthogonal inner product is used to impose continuity conditions on the artificial vertical surface and the edge conditions at the crack. The derived formulation is not just limited to the circular crack problem but can also be readily used in a variety of other problems, including wave diffraction by a surface-piercing vertical cylinder, polynya and circular disc floating on the free surface in a channel. Extensive results are provided for the forces on the inner ice sheet, the transmission and reflection coefficients. In particular, a detailed analysis is made on their behaviours near the natural frequencies of the channel, and the natural frequencies corresponding to the motion of the inner ice sheet.

1. Introduction

The topic of water wave interaction with floating ice sheets has been received considerable attention in the past few decades. On one hand, water wave propagating in polar regions may cause seasonal changes on the morphology of the ice cover and distribution, which could have a significant impact on the polar environment (Collins III et al., 2015). On the other hand, from the aspect of polar engineering, understanding the behaviour of wave in icy water regions can provide some important insights into the nature of its interaction with offshore structures. Ice may appear in different forms in polar regions. If the horizontal dimension of an ice sheet is much larger than its thickness, the ice sheet may be modelled as a thin elastic plate (Ewing and Crary, 1934). By applying the Kirchhoff-Love plate theory and linearized potential flow theory, Fox and Squire (1994) studied the reflection and transmission of an oblique incident wave into a semi-infinite ice sheet based on the method of matched eigenfunction expansions (MEE). Later, the problem was considered by Balmforth and Craster (1999) through the Wiener-Hopf technique, while the ice sheet was described by the Timoshenko-Mindlin equation. Sturova (1999) used the MEE procedure to investigate the diffraction of an oblique incoming wave by

* Corresponding author.
E-mail address: g.wu@ucl.ac.uk (G.X. Wu).

https://doi.org/10.1016/j.jfluidstructs.2024.104173
Received 2 March 2024; Received in revised form 3 June 2024; Accepted 21 August 2024

an ice sheet with finite width. When the length of the ice sheet is not sufficiently large, it becomes a fully three-dimensional problem. Meylan and Squire (1996) studied the problem of water wave diffraction by a floating circular ice floe through a combination of the methods of MEE and Green function. Wang and Meylan (2004) solved the wave diffraction problem of ice floe with arbitrary shapes, where the boundary element method (BEM) was used for the flow, and the finite element method (FEM) for the ice sheet. Similar work was also one by Montiel et al. (2013) for water wave interaction with one and multiple floating elastic discs through the method of MEE. A more recent work was that by Porter (2019) based on Fourier transform and Rayleigh-Ritz method to study the interaction between water waves and single and multiple rectangular floating ice sheets.

In reality, ice sheets typically exhibit imperfections and various defects, among which cracks are common occurrences. When incoming water waves interact with these cracks, significant stress and strain may occur within the ice sheet, particularly in the vicinity of the ice edge, which can promote the propagation of fractures, result in for example some sea ice leads. Squire and Dixon (2000) derived an analytical solution of waves propagation through an ice sheet with a solitary crack. Later, Williams and Squire (2002) extended it to oblique incident waves. The finite water depth problem was solved by Evans and Porter (2003) through the methods of vertical mode expansion and Green function. The approach was then employed by Porter and Evans (2006) to study wave diffraction by multiple parallel straight cracks. Through expanding the jumps of deflection and slope at the crack into Chebyshev polynomials, Porter and Evans (2007) extended the problem to cracks with finite length. A similar problem was also considered by Marchenko (1993) and Williams and Squire (2006) based on the Wiener-Hopf technique and residue calculus, respectively. In their works, ice sheets of different properties on both sides of the crack were considered. In addition to straight cracks, closed curved cracks, also referred to as crevasses (Jansson et al., 2007) can also form on ice sheets. When water waves interact with a closed curved crack, one of the effects is that the excess of the stress or fatigue may have the potential to cause disintegration of the ice sheet in the affected area. A relevant example is the breakup of the Wilkins Ice Shelf (Anon., NASA, 2013). Also, water waves may cause large vertical movement and deflection of the ice sheet inside of the closed crack, which is similar to the motion of an ice floe (Squire et al., 1995), although its horizontal movement is restricted by the external ice sheet. The motion of the inner ice sheet may pose risks in some geographic observations and measurements near the ice cracks (Lazzara et al., 1999). Li et al. (2018) investigated the problem of water wave diffraction by a circular crack in an ice sheet floating on the water of finite depth. In their work, the Green function without the crack was first derived in an integral form. Then the diffraction potential was constructed from the boundary integral equation and the solution was obtained analytically. Mandal et al. (2018) studied a more general case by the method of vertical mode expansion, where different properties of ice sheets inside and outside the circular crack were considered. Later, Li et al. (2020) proposed a numerical approach and further extended the problem to wave diffraction by multiple cracks of arbitrary shapes. In some cases, the cracks may not be very narrow, and polynya or lead may appear. Relevant works can be found in Chung and Linton (2005) for the transmission and reflection of waves across a lead between two semi-infinite ice sheets, Bennetts and Williams (2010) for wave scattering by polynyas of arbitrary shapes, and Shi et al. (2019) for wave interaction with multiple wide-spaced polynyas.

In ocean engineering it is common to use wave tanks to undertake model tests to understand the nature of the waves and their interactions with structures. The tank is usually long, and measures are usually put at the far end to minimize wave reflection. It is therefore often treated as infinitely long channel. However, the width of the tank is often limited, and its effects on the wave and the behaviour of the structure may be important. To use the results from model test for the real ocean, it is important to understand the nature of the side wall effects. The problem of a hydroelastic wave propagating along a channel fully covered by a homogeneous ice sheet was considered by Korobkin et al. (2014) and Ren et al. (2020). Their results suggested that the progressing waves in the channel are always three–dimensional because of the effect of the ice sheet edge constrains on the channel walls. Using a similar procedure in Korobkin et al. (2014), Shishmarev et al. (2016) and Khabakhpasheva et al. (2019) studied the wave generated by a load moving steadily on the surface of an ice sheet. Yang et al. (2021) investigated the hydroelastic waves due to a uniform current passing a submerged horizontal circular cylinder in a channel with an ice cover, which is related to the problem of a submerged body at forward speed. Furthermore, Yang et al. (2022) employed the method of vertical modes expansion for the Green function in the channel and used it to solve the problem of wave diffraction by a vertical circular cylinder standing in an ice-covered channel.

Here, although the approach of Yang et al. (2022) is used, the boundary integral equation has been derived for general cases. The vertical cylinder problem in the work of Yang et al. (2022) is only one of the special cases. Based on this more general formation, a variety of problems, including wave diffraction by cracks in an ice sheet, polynya, and discs floating on the free surface are investigated in the paper. The distribution of the natural frequencies of the tank is rigorously established. Previous work has provided only an implicit equation in the form of an infinite series for the natural frequencies. The solutions were obtained through a numerical search. It is not too clear where the roots are and whether the search has missed some roots. It has shown clearly here how the roots of the dispersion equation for waves in an ice-covered channel are distributed and the bound of each root. Also, the infinite series of the dispersion relationship does not converge when the thickness of the ice sheet is taken to be zero, and therefore the equation cannot be used directly in such a case. We have then shown that the roots, or the natural frequencies, tend to those of the free surface as the thickness tends to zero and this means that the result of the free surface is recovered by the present formulation. Detailed analysis is made on the transmission and reflection coefficients, hydrodynamic forces on the inner ice sheet, and sloshing motion of fluid in polynya in the tank. The reasons of sharp variation of physical results with the wave frequency are explained, especially associated with the natural frequencies of the channel, and the natural frequencies of the motion of the inner ice sheet, natural frequencies of sloshing motion in the polynya as well as various edge conditions. Besides, the procedure here can be also used to solve problems of arbitrary shapes by employing numerical discretization.

The paper is organized as follows. The mathematical model is introduced in Section. 2. Formulations for the velocity potential of incident wave are described in Section 3.1. The total velocity potentials in the inner and outer domains are constructed in Section. 3.2.

The far-field behaviour of the wave is discussed in Section 3.3. In Section 3.4, the formulas of hydrodynamic forces on the inner ice sheet are derived. The numerical results are presented in Section. 4. Conclusions are given in Section. 5.

2. Mathematical model

We use the case of wave propagation in a channel covered by an imperfect ice sheet, or ice sheet with a crack to derive the formulation. Although the procedure used can be readily applied to a crack of an arbitrary shape, we focus on a circular one. The cross section of the channel is rectangular and its width $2b$ and mean water depth H are constant, as sketched in Fig. 1. The ice sheet is divided into two parts by the circular crack, each part of the ice sheet is assumed to have uniform density and thickness, or ρ_1 and h_1 for the outside ice sheet, ρ_2 and h_2 for the inside ice sheet. A Cartesian coordinate system $O-xyz$ is defined with the origin located at the central plane of the channel and the lower surface of the ice sheet, the x-axis points in the longitudinal direction of the channel and z-axis points upwards. The centre of the circular crack with radius a is located at $(x_c, y_c, 0)$. An incoming wave that comes from $x=+\infty$ will be diffracted by the crack.

A cylindrical coordinate system (r,θ,z) with the origin at the centre of the crack is further introduced as

$$\left.\begin{array}{l} x-x_c = r\cos\theta \\ y-y_c = r\sin\theta \end{array}\right\}. \tag{1}$$

The fluid with density ρ is assumed to be inviscid and incompressible and homogeneous, and its motion is irrotational. Thus, the velocity potential $\Phi(x,y,z,t)$ can be adopted to describe the flow field. When the amplitude of the wave is small compared with its length, linearization can be further introduced. When the motion is sinusoidal in time with radian frequency ω, the total velocity potential can be expressed as

$$\Phi(x,y,z,t) = Re\left\{\phi(x,y,z)\times e^{i\omega t}\right\}. \tag{2}$$

where $\phi(x,y,z)$ is due to incident and diffracted waves. The conservation of mass requires ϕ to satisfy the Laplace equation

$$\nabla^2\phi + \frac{\partial^2\phi}{\partial z^2} = 0,\ -\infty < x < +\infty,\ -b \le y \le b,\ -H \le z \le 0, \tag{3}$$

where $\nabla^2 = \frac{\partial^2}{\partial x^2} + \frac{\partial^2}{\partial y^2}$ denotes the two-dimensional Laplacian in the horizontal plane. The ice sheet is modelled by the Kirchhoff-Love theory for an elastic plate. Assuming that there is no air gap between the ice sheet and the water surface, the boundary condition there can be written as

$$\left(L_i\nabla^4 - m_i\omega^2 + \rho g\right)\frac{\partial\phi}{\partial z} - \rho\omega^2\phi = 0,\ z=0,\ \begin{cases} i=1:\ r<a \\ i=2:\ r>a \end{cases}. \tag{4}$$

where $L_i = E_i h_i^3/\left[12\left(1-\nu_i^2\right)\right], E_i$ and ν_i $(i=1,\ 2)$ represent the flexural rigidity, Young's modulus and Poisson's ratio of the sheet respectively, $m_i = \rho_i h_i$ denotes the mass per unit area of the ice sheet, g denotes the gravitational acceleration. $i=1,\ 2$ here correspond to the outer and inner ice sheets respectively. At the two side walls and the bottom of the channel, the impermeable condition gives

$$\frac{\partial\phi}{\partial y} = 0,\ y=\pm b, \tag{5}$$

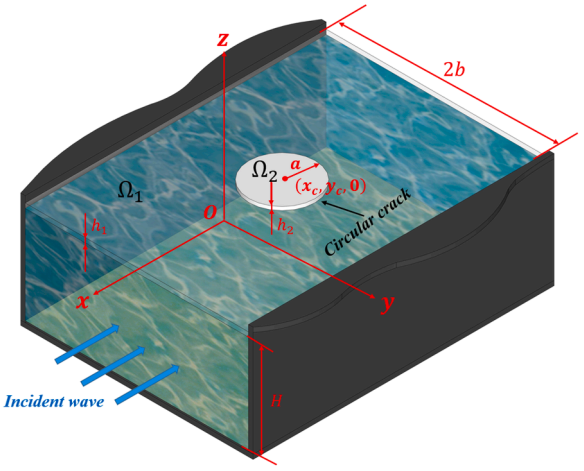

Fig. 1. The sketch of the problem.

$$\frac{\partial \phi}{\partial z} = 0,\ z = -H, \tag{6}$$

We assume that the ice sheets on two sides of the circular crack are fully detached, which means that the conditions of zero bending moment and shear force should be enforced (Timoshenko and Woinowsky-Krieger, 1959)

$$\mathscr{B}\left(\frac{\partial \phi}{\partial z}\right) = 0 \text{ and } \mathscr{S}\left(\frac{\partial \phi}{\partial z}\right) = 0,\ r = a,\ z = 0, \tag{7a, b}$$

where the operators $\mathscr{B}$ and $\mathscr{S}$ are defined as

$$\left.\begin{aligned} \mathscr{B} &= \nabla^2 - \frac{\nu_i'}{a}\left(\frac{1}{a}\frac{\partial^2}{\partial \theta^2} + \frac{\partial}{\partial r}\right) \\ \mathscr{S} &= \frac{\partial}{\partial r}\nabla^2 + \frac{\nu_i'}{a^2}\left(\frac{\partial^3}{\partial r \partial \theta^2} - \frac{1}{a}\frac{\partial^2}{\partial \theta^2}\right) \end{aligned}\right\}, \tag{8a, b}$$

and $\nu_i' = 1 - \nu_i$. For the edge conditions at the intersection lines of the ice sheet with two side walls, we consider two common types

$$\left.\begin{aligned} \frac{\partial \phi}{\partial z} = 0,\ \frac{\partial^2 \phi}{\partial y \partial z} = 0 \qquad & \text{Clamped} \\ \frac{\partial^3 \phi}{\partial y^2 \partial z} + \nu \frac{\partial^3 \phi}{\partial x^2 \partial z} = 0,\ \frac{\partial^4 \phi}{\partial y^3 \partial z} + (2-\nu)\frac{\partial^4 \phi}{\partial x^2 \partial y \partial z} = 0 \qquad & \text{Free} \end{aligned}\right\},\ y = \pm b, z = 0. \tag{9a, b}$$

In addition, at $x = \pm\infty$, the far-field radiation conditions should be imposed to ensure that the disturbed wave propagates outwards.

3. Solution procedure

The fluid domain is divided into two parts, as given in Fig. 1, namely the outer domain Ω_1 $(r > a)$ and the inner domain Ω_2 $(r < a)$. The velocity potential in Ω_i $(i = 1,\ 2)$ is defined as $\phi^{(i)}$. $\phi^{(1)}$ can be further written as $\phi^{(1)} = \phi_I + \phi_D^{(1)}$, where ϕ_I and $\phi_D^{(1)}$ denote the incident and diffraction potential respectively. Here, $\phi_D^{(1)}$ is constructed by a boundary integral equation, and $\phi^{(2)}$ is established through the eigenfunction expansion.

3.1. The velocity potential of an incoming wave in an ice-covered channel

The velocity potential of an incoming wave in an ice-covered channel can be written as (Yang et al., 2022),

$$\phi_I(x,y,z) = \mathrm{i}\omega \frac{A}{\chi(k_0)} \times e^{-\mathrm{i}k_0(x-x_c)} \times \sum_{m=-2}^{+\infty} \frac{I_m(k_0)\psi_m(z)}{Q_m} \frac{\cos[\sigma_m(k_0)y]}{\sin[\sigma_m(k_0)b]}, \tag{10}$$

where $\psi_m(z)$, Q_m, $I_m(k)$ and $\sigma_m(k)$ have been introduced in Appendix. A,

$$\chi(k_0) = \sum_{m=-2}^{+\infty} \frac{I_m(k_0)\kappa_m \tanh \kappa_m H}{Q_m \sin[\sigma_m(k_0)b]}, \tag{11}$$

A in Eq. (10) denotes the amplitude of the wave at $y = 0$. k_0 is the largest positive real root of $\mathscr{T}_S(k,\omega) = 0$, as discussed in Appendix. A.

3.2. The velocity potentials in the inner and outer domains

Through applying the Green's second identity to G and $\phi_D^{(1)}$, we may have

$$\Lambda \phi_D^{(1)}(x,y,z) = \iint_S \left[\phi_D^{(1)}(x_0,y_0,z_0)\frac{\partial G(x,y,z,x_0,y_0,z_0)}{\partial n_0} - G(x,y,z,x_0,y_0,z_0)\frac{\partial \phi_D^{(1)}(x_0,y_0,z_0)}{\partial n_0}\right] dS_0, \tag{12}$$

where S is comprised of the bottom of the channel S_H, two vertical channel walls S_W, the entire outer ice sheet S_I, two vertical far-field surfaces $S_{\pm\infty}$ at $x = \pm\infty$ and a vertical surface at $r = a$. Λ in Eq. (12) is the solid angle at the field point (x,y,z). Since all the boundaries here are smooth, $\Lambda = 2\pi$ if $(x,y,z)$is at the boundary, otherwise $\Lambda = 4\pi$. $G(x,y,z,x_0,y_0,z_0)$ denotes the Green function for a rectangular channel fully covered by a homogeneous ice sheet (Yang et al., 2022), which is given in detail in Appendix. A. Noticing that the Green function in Eq. (A1) satisfies all the boundary conditions apart from that at $r = a$. In such a case, Eq. (12) can be further simplified to the following formula Yang et al. (2022) of source distribution over $r = a$

$$\phi_D^{(1)}(x,y,z) = a\int_0^{2\pi} \langle G(x,y,z;x_0,y_0,z_0), \Psi(x_0,y_0,z_0)\rangle d\theta_0. \tag{13}$$

where Ψ is the strength of the source distributed over the interface at $r=a,\ x_0-x_c=a\cos\theta_0$ and $y_0-y_c=a\sin\theta_0$ (Yang et al., 2022). The operator $\langle\rangle$ is defined as

$$\langle G,\Psi\rangle = \int_{-H}^{0} G\Psi dz + \frac{L_1}{\rho\omega^2}\left(\frac{\partial G}{\partial z}\frac{\partial^3\Psi}{\partial z^3} + \frac{\partial^3 G}{\partial z^3}\frac{\partial\Psi}{\partial z}\right)\Big|_{z=0}. \tag{14}$$

Following Eq. (14), we may consider

$$I_{m,\tilde{m}} = \frac{1}{\kappa_m^2-\kappa_{\tilde{m}}^2}\int_{-H}^{0}\left[\psi_m''(z)\psi_{\tilde{m}}(z) - \psi_m(z)\psi_{\tilde{m}}''(z)\right]dz,\ m\neq\tilde{m}. \tag{15}$$

$\psi_m(z)$ is defined in Eq. (A2), which provides $\psi_m''(z)=\kappa_m^2\psi_m(z),\ \psi_{\tilde{m}}''(z)=\kappa_{\tilde{m}}^2\psi_{\tilde{m}}(z)$, and then Eq. (15) gives

$$I_{m,\tilde{m}} = \int_{-H}^{0}\psi_m(z)\psi_{\tilde{m}}(z)dz. \tag{16}$$

Applying the integration by parts to Eq. (15), we obtain

$$I_{m,\tilde{m}} = \frac{\psi_m'(0)\psi_{\tilde{m}}(0) - \psi_{\tilde{m}}'(0)\psi_m(0)}{\kappa_m^2-\kappa_{\tilde{m}}^2}. \tag{17}$$

Using the ice sheet boundary condition in Eq. (4), we have

$$\left.\begin{aligned}\psi_m(0) &= \frac{L_1}{\rho\omega^2}\psi_m^{(\mathrm{IV})}(0) + \frac{\rho g - m_1\omega^2}{\rho\omega^2}\psi_m'(0)\\ \psi_{\tilde{m}}(0) &= \frac{L_1}{\rho\omega^2}\psi_{\tilde{m}}^{(\mathrm{IV})}(0) + \frac{\rho g - m_1\omega^2}{\rho\omega^2}\psi_{\tilde{m}}'(0)\end{aligned}\right\}. \tag{18a, b}$$

Substituting Eq. (18) into Eq. (17), we obtain

$$I_{m,\tilde{m}} = \frac{L_1}{\rho\omega^2}\frac{\psi_m'(0)\psi_{\tilde{m}}^{(\mathrm{IV})}(0) - \psi_m^{(\mathrm{IV})}(0)\psi_{\tilde{m}}'(0)}{\kappa_m^2-\kappa_{\tilde{m}}^2}. \tag{19}$$

Using $\psi_m^{(\mathrm{IV})}(0)=\kappa_m^4\psi_m'(0)$ and $\psi_{\tilde{m}}^{(\mathrm{IV})}(0)=\kappa_{\tilde{m}}^4\psi_{\tilde{m}}'(0)$, Eq. (19) can be further expressed as

$$I_{m,\tilde{m}} = -\frac{L_1}{\rho\omega^2}\left(\kappa_m^2+\kappa_{\tilde{m}}^2\right)\psi_m'(0)\psi_{\tilde{m}}'(0) = -\frac{L_1}{\rho\omega^2}\left(\frac{d^3\psi_m}{dz^3}\frac{d\psi_{\tilde{m}}}{dz} + \frac{d\psi_m}{dz}\frac{d^3\psi_{\tilde{m}}}{dz^3}\right)_{z=0}. \tag{20}$$

From Eqs. (16) and (20), we obtain

$$\int_{-H}^{0}\psi_m(z)\psi_{\tilde{m}}(z)dz + \frac{L_1}{\rho\omega^2}\left(\frac{d^3\psi_m}{dz^3}\frac{d\psi_{\tilde{m}}}{dz} + \frac{d\psi_m}{dz}\frac{d^3\psi_{\tilde{m}}}{dz^3}\right)_{z=0} = 0,\ m\neq\tilde{m}. \tag{21}$$

When $m=\tilde{m}$, the left-hand side of Eq. (21) can be found to be equal to Q_m given in Eq. (A3). Thus, we may have the following orthogonal product for the vertical mode $\psi_m(z)$,

$$\langle\psi_m,\psi_{\tilde{m}}\rangle = \int_{-H}^{0}\psi_m\psi_{\tilde{m}}dz + \frac{L_1}{\rho\omega^2}\left(\frac{d\psi_m}{dz}\frac{d^3\psi_{\tilde{m}}}{dz^3} + \frac{d^3\psi_m}{dz^3}\frac{d\psi_{\tilde{m}}}{dz}\right)\Big|_{z=0} = \delta_{m\tilde{m}}Q_m \tag{22}$$

as given by Sahoo et al. (2001), where $\delta_{m\tilde{m}}$ denotes the Kronecker delta function.

To obtain $\phi_D^{(1)}$, Ψ may be expressed into a double series in the cylindrical coordinate (a,θ_0,z_0) as

$$\Psi(a,\theta_0,z_0) = \frac{1}{4\pi a}\sum_{n=-\infty}^{+\infty}\sum_{m=-2}^{+\infty}\frac{a_{n,m}}{Q_m\mathscr{J}_n(\kappa_m a)}\times\psi_m(z_0)e^{-in\theta_0}, \tag{23}$$

where $a_{n,m}$ are unknown coefficients, and $\mathscr{J}_n$ represents the n-th Bessel function of the first kind.

From Abramowitz and Stegun (1965), we write

$$\left.\begin{aligned}\mathscr{H}_0^{(2)}(\kappa_m R) &= \sum_{n=-\infty}^{+\infty}\mathscr{H}_n^{(2)}(\kappa_m r)\mathscr{J}_n(\kappa_m r_0)e^{\mathrm{i}n(\theta_0-\theta)}\\ e^{\mathrm{i}\left[\sigma_m(y_0-y_c)\pm k(x_0-x_c)\right]} &= \sum_{n=-\infty}^{+\infty}\mathscr{J}_n(\kappa_m r_0)e^{\mathrm{i}n(\theta_0\pm\gamma_m)}\\ e^{\mathrm{i}\left[-\sigma_m(y_0-y_c)\pm k(x_0-x_c)\right]} &= \sum_{n=-\infty}^{+\infty}(-1)^n\mathscr{J}_n(\kappa_m r_0)e^{\mathrm{i}n(\theta_0\mp\gamma_m)}\end{aligned}\right\}. \tag{24a, b, c}$$

The Green function in Eq. (A1) becomes

$$\begin{aligned}G(x,y,z;r_0,\theta_0,z_0) = {}& \frac{\mathrm{i}\pi}{2}\sum_{n=-\infty}^{+\infty}\sum_{m=-2}^{+\infty}\frac{\psi_m(z)\psi_m(z_0)}{Q_m}\mathscr{H}_n^{(2)}(\kappa_m r)\mathscr{J}_n(\kappa_m r_0)e^{\mathrm{i}n(\theta_0-\theta)}+\\ &\sum_{n=-\infty}^{+\infty}\sum_{m=-2}^{+\infty}\frac{\psi_m(z)\psi_m(z_0)}{Q_m}\left\{\int_0^{+\infty}\left[\begin{array}{l}\dfrac{\left[E_{n,m}(k,y_c)e^{-\mathrm{i}k(x-x_c)}+E_{-n,m}(k,y_c)e^{\mathrm{i}k(x-x_c)}\right]\cos\sigma_m y}{2\sigma_m\sin\sigma_m b}\\ -i\dfrac{\left[F_{n,m}(k,y_c)e^{-\mathrm{i}k(x-x_c)}+F_{-n,m}(k,y_c)e^{\mathrm{i}k(x-x_c)}\right]\sin\sigma_m y}{2\sigma_m\cos\sigma_m b}\end{array}\right]e^{-\mathrm{i}\sigma_m b}dk\right\}\times\mathscr{J}_n(\kappa_m r_0)e^{\mathrm{i}n\theta_0}+\\ &\sum_{n=-\infty}^{+\infty}\sum_{m=-2}^{+\infty}\sum_{m'=-2}^{+\infty}\frac{\psi_{m'}(z)\psi_m(z_0)}{Q_{m'}Q_m}\left\{\int_\ell I_m(k)I_{m'}(k)\left[\begin{array}{l}\dfrac{\left[E_{n,m}(k,y_c)e^{-\mathrm{i}k(x-x_c)}+E_{-n,m}(k,y_c)e^{\mathrm{i}k(x-x_c)}\right]\cos\sigma_{m'}y}{\mathscr{T}_S(k,\omega)\sin\sigma_{m'}b\sin\sigma_m b}\\ +\dfrac{\left[F_{n,m}(k,y_c)e^{-\mathrm{i}k(x-x_c)}+F_{-n,m}(k,y_c)e^{\mathrm{i}k(x-x_c)}\right]\sin\sigma_{m'}y}{\mathscr{T}_A(k,\omega)\cos\sigma_{m'}b\cos\sigma_m b}\end{array}\right]dk\right\}\times\mathscr{J}_n(\kappa_m r_0)e^{\mathrm{i}n\theta_0}\end{aligned}, \tag{25}$$

where

$$\left.\begin{aligned}E_{n,m}(k,y_c) &= e^{\mathrm{i}\frac{n\pi}{2}}\cos\left(\sigma_m y_c+n\gamma_m-\frac{n\pi}{2}\right)\\ F_{n,m}(k,y_c) &= e^{\mathrm{i}\frac{n\pi}{2}}\sin\left(\sigma_m y_c+n\gamma_m-\frac{n\pi}{2}\right)\end{aligned}\right\}. \tag{26a,b}$$

$$\left.\begin{aligned}k &= \kappa_m\sin\gamma_m\\ \sigma_m &= \kappa_m\cos\gamma_m\end{aligned}\right\}. \tag{27a,b}$$

Substituting Eqs. (23) and (25) into Eq. (13), we obtain

$$\begin{aligned}\phi_D^{(1)}(x,y,z) = {}& \frac{\mathrm{i}\pi}{2}\sum_{n=-\infty}^{+\infty}\sum_{m=-2}^{+\infty}a_{n,m}\times\frac{\psi_m(z)}{Q_m}\mathscr{H}_n^{(2)}(\kappa_m r)e^{-\mathrm{i}n\theta}\\ &+\sum_{n=-\infty}^{+\infty}\sum_{m=-2}^{+\infty}a_{n,m}\times\frac{\psi_m(z)}{Q_m}\left\{\int_0^{+\infty}\left[\begin{array}{l}\dfrac{\left[E_{n,m}(k,y_c)e^{-\mathrm{i}k(x-x_c)}+E_{-n,m}(k,y_c)e^{\mathrm{i}k(x-x_c)}\right]\cos\sigma_m y}{2\sigma_m\sin\sigma_m b}\\ -i\dfrac{\left[F_{n,m}(k,y_c)e^{-\mathrm{i}k(x-x_c)}+F_{-n,m}(k,y_c)e^{\mathrm{i}k(x-x_c)}\right]\sin\sigma_m y}{2\sigma_m\cos\sigma_m b}\end{array}\right]e^{-\mathrm{i}\sigma_m b}dk\right\}\\ &+\sum_{n=-\infty}^{+\infty}\sum_{m=-2}^{+\infty}\sum_{m'=-2}^{+\infty}a_{n,m}\times\frac{\psi_{m'}(z)}{Q_{m'}Q_m}\left\{\int_\ell I_m(k)I_{m'}(k)\left[\begin{array}{l}\dfrac{\left[E_{n,m}(k,y_c)e^{-\mathrm{i}k(x-x_c)}+E_{-n,m}(k,y_c)e^{\mathrm{i}k(x-x_c)}\right]\cos\sigma_{m'}y}{\mathscr{T}_S(k,\omega)\sin\sigma_{m'}b\sin\sigma_m b}\\ +\dfrac{\left[F_{n,m}(k,y_c)e^{-\mathrm{i}k(x-x_c)}+F_{-n,m}(k,y_c)e^{\mathrm{i}k(x-x_c)}\right]\sin\sigma_{m'}y}{\mathscr{T}_A(k,\omega)\cos\sigma_{m'}b\cos\sigma_m b}\end{array}\right]dk\right\}.\end{aligned} \tag{28}$$

To impose the boundary condition at $r=a$ and edge conditions at $r=a$, $z=0$ on $\phi_D^{(1)}$, we may apply Eqs. (24b, c) to Eq. (28), which provides

$$\begin{aligned}\phi_D^{(1)}(r,\theta,z) = {}& \frac{\mathrm{i}\pi}{2}\sum_{n=-\infty}^{+\infty}\sum_{m=-2}^{+\infty}a_{n,m}\times\frac{\psi_m(z)}{Q_m}\mathscr{H}_n^{(2)}(\kappa_m r)e^{-\mathrm{i}n\theta}+\sum_{n=-\infty}^{+\infty}\sum_{n'=-\infty}^{+\infty}\sum_{m=-2}^{+\infty}a_{n,m}\mathscr{C}_{n,n',m}\psi_m(z)\mathscr{J}_{n'}(\kappa_m r)e^{\mathrm{i}n'\theta}\\ &+\sum_{n=-\infty}^{+\infty}\sum_{n'=-\infty}^{+\infty}\sum_{m=-2}^{+\infty}\sum_{m'=-2}^{+\infty}a_{n,m}\mathscr{D}_{n,n',m,m'}\psi_{m'}(z)\mathscr{J}_{n'}(\kappa_{m'}r)e^{\mathrm{i}n'\theta},\end{aligned} \tag{29}$$

where

$$\mathscr{C}_{n,n',m}=\frac{1}{Q_m}\int_0^{+\infty}\left[\begin{array}{l}\dfrac{E_{n,m}(k,y_c)E_{-n',m}(k,y_c)+E_{-n,m}(k,y_c)E_{n',m}(k,y_c)}{2\sigma_m\sin\sigma_m b}\\ -i\dfrac{F_{n,m}(k,y_c)F_{-n',m}(k,y_c)+F_{-n,m}(k,y_c)F_{n',m}(k,y_c)}{2\sigma_m\cos\sigma_m b}\end{array}\right]e^{-i\sigma_m b}dk, \tag{30}$$

$$\mathscr{D}_{n,n',m,m'}=\frac{1}{Q_mQ_{m'}}\int_{\mathscr{C}}I_m(k)\,I_{m'}(k)\left[\begin{array}{l}\dfrac{E_{n,m}(k,y_c)E_{-n',m'}(k,y_c)+E_{-n,m}(k,y_c)E_{n',m'}(k,y_c)}{\mathscr{F}_S(k,\omega)\sin\sigma_m b\sin\sigma_{m'}b}\\ +\dfrac{F_{n,m}(k,y_c)F_{-n',m'}(k,y_c)+F_{-n,m}(k,y_c)F_{n',m'}(k,y_c)}{\mathscr{F}_A(k,\omega)\cos\sigma_m b\cos\sigma_{m'}b}\end{array}\right]dk, \tag{31}$$

ϕ_I in Eq. (10) can also be written in the cylindrical system in the following form

$$\phi_I(r,\theta,z)=i\omega\frac{A}{\chi(k_0)}\times\sum_{n=-\infty}^{+\infty}\sum_{m=-2}^{+\infty}\frac{I_m(k_0)\psi_m(z)}{Q_m}\frac{E_{-n,m}(k_0,y_c)}{\sin[\sigma_m(k_0)b]}\mathscr{J}_n(\kappa_m r)e^{in\theta}. \tag{32}$$

In the inner domain Ω_2, from Ren et al. (2021), $\phi^{(2)}$ can be written as

$$\phi^{(2)}(r,\theta,z)=\sum_{n=-\infty}^{+\infty}\sum_{m=-2}^{+\infty}b_{n,m}\mathscr{J}_n(\mathscr{k}_m r)\varphi_m(z)e^{in\theta}, \tag{33}$$

where

$$\varphi_m(z)=\frac{\cosh\mathscr{k}_m(z+H)}{\cosh(\mathscr{k}_m H)}, \tag{34}$$

and $b_{n,m}$ are unknown coefficients. Similar to κ_m, $\alpha=\mathscr{k}_m$ are defined as the roots of $K_2(\alpha,\omega)=0$, where

$$K_2(\alpha,\omega)=\left(L_2\alpha^4+\rho g-m_2\omega^2\right)\alpha\sinh\alpha H-\rho\omega^2\cosh\alpha H. \tag{35}$$

In particular, $\mathscr{k}_{-2}$ and $\mathscr{k}_{-1}$ are two complex roots with negative imaginary parts and $\mathscr{k}_{-2}=-\overline{\mathscr{k}}_{-1}$, $\mathscr{k}_0$ is the purely positive real root, $\mathscr{k}_m(m=1,2,3,\cdots)$ are an infinite number of purely negative imaginary roots. $\varphi_m(z)$ also satisfies the following inner product as

$$\langle\varphi_m,\varphi_{\tilde{m}}\rangle=\int_{-H}^{0}\varphi_m\varphi_{\tilde{m}}dz+\frac{L_2}{\rho\omega^2}\left(\frac{d\varphi_m}{dz}\frac{d^3\varphi_{\tilde{m}}}{dz^3}+\frac{d^3\varphi_m}{dz^3}\frac{d\varphi_{\tilde{m}}}{dz}\right)\Bigg|_{z=0}=\delta_{m\tilde{m}}P_m, \tag{36}$$

where

$$P_m=\frac{2\mathscr{k}_m H+\sinh(2\mathscr{k}_m H)}{4\mathscr{k}_m\cosh^2(\mathscr{k}_m H)}+\frac{2L_2}{\rho\omega^2}\mathscr{k}_m^4\tanh^2(\mathscr{k}_m H). \tag{37}$$

On the surface of $r=a$, the pressure and velocity of the fluid should be continuous, or

$$\phi^{(1)}(a,\theta,z)=\phi^{(2)}(a,\theta,z)\ \text{and}\ \frac{\partial\phi^{(1)}(a,\theta,z)}{\partial r}=\frac{\partial\phi^{(2)}(a,\theta,z)}{\partial r}, \tag{38a, b}$$

Applying the inner products in Eqs. (22) and (36), and using Eq. (38), we have

$$\left\langle\frac{\partial\phi^{(1)}}{\partial r},\psi_m\right\rangle=\int_{-H}^{0}\frac{\partial\phi^{(2)}}{\partial r}\psi_m dz+\frac{L_1}{\rho\omega^2}\left(\frac{d\psi_m}{dz}\frac{\partial^4\phi^{(1)}}{\partial r\partial z^3}+\frac{d^3\psi_m}{dz^3}\frac{\partial^2\phi^{(1)}}{\partial r\partial z}\right)\Bigg|_{z=0}, \tag{39}$$

$$\langle\phi^{(2)},\varphi_m\rangle=\int_{-H}^{0}\phi^{(1)}\varphi_m dz+\frac{L_2}{\rho\omega^2}\left(\frac{d\varphi_m}{dz}\frac{\partial^3\phi^{(2)}}{\partial z^3}+\frac{d^3\varphi_m}{dz^3}\frac{\partial\phi^{(2)}}{\partial z}\right)\Bigg|_{z=0}. \tag{40}$$

Substituting Eqs. (29), (32) and (33) into Eqs. (39) and (40), and define

$$\left.\begin{aligned}
\frac{\partial^2\phi^{(1)}}{\partial r\partial z} &= -\sum_{n=-\infty}^{+\infty} c_n e^{in\theta}\\
\frac{\partial^4\phi^{(1)}}{\partial r\partial z^3} &= -\sum_{n=-\infty}^{+\infty} d_n e^{in\theta}\\
\frac{\partial\phi^{(2)}}{\partial z} &= -\sum_{n=-\infty}^{+\infty} e_n e^{in\theta}\\
\frac{\partial^3\phi^{(2)}}{\partial z^3} &= -\sum_{n=-\infty}^{+\infty} f_n e^{in\theta}
\end{aligned}\right\}, \tag{41a-d}$$

where c_n, d_n, e_n and f_n are unknown coefficients. A system of linear equations of the following form can be obtained as

$$\begin{aligned}
&\frac{i\pi}{2}\frac{(-1)^n\mathscr{H}_n^{(2)'}(\kappa_m a)}{Q_m\mathscr{J}'_n(\kappa_m a)}a_{-n,m} + \sum_{n'=-\infty}^{+\infty}\mathscr{C}_{n',n,m}a_{n',m} + \sum_{n'=-\infty}^{+\infty}\sum_{m'=-2}^{+\infty}\mathscr{D}_{n',n,m',m}a_{n',m'} - \sum_{m'=-2}^{+\infty}\frac{X(\kappa_m,\ell_{m'})\ell_{m'}\mathscr{J}'_n(\ell_{m'}a)}{Q_m\kappa_m\mathscr{J}'_n(\kappa_m a)}b_{n,m'}\\
&\quad + \frac{L_1\tanh\kappa_m H}{\rho\omega^2 Q_m\mathscr{J}'_n(\kappa_m a)}(\kappa_m^2 c_n + d_n)\\
&\quad = -i\frac{\omega A I_m(k_0)E_{-n,m}(k_0,y_c)}{Q_m\chi(k_0)\sin[\sigma_m(k_0)b]},
\end{aligned} \tag{42}$$

$$\begin{aligned}
&b_{n,m} - \frac{i\pi}{2}\sum_{m'=-2}^{+\infty}\frac{(-1)^n X(\ell_m,\kappa_{m'})\mathscr{H}_n^{(2)}(\kappa_{m'}a)}{Q_{m'}P_m\mathscr{J}_n(\ell_m a)}a_{-n,m'}\\
&\quad - \sum_{n'=-\infty}^{+\infty}\sum_{m'=-2}^{+\infty}\frac{X(\ell_m,\kappa_{m'})\mathscr{J}_n(\kappa_{m'}a)}{P_m\mathscr{J}_n(\ell_m a)}\mathscr{C}_{n',n,m'}a_{n',m'} -\\
&\sum_{n'=-\infty}^{+\infty}\sum_{m'=-2}^{+\infty}\sum_{m''=-2}^{+\infty}\frac{X(\ell_m,\kappa_{m'})\mathscr{J}_n(\kappa_{m'}a)}{P_m\mathscr{J}_n(\ell_m a)}\mathscr{D}_{n',n,m'',m'}a_{n',m''} + \frac{L_2\ell_m\tanh\ell_m H}{\rho\omega^2 P_m\mathscr{J}_n(\ell_m a)}(\ell_m^2 e_n + f_n)\\
&\quad = i\frac{\omega A}{\chi(k_0)}\sum_{m'=-2}^{+\infty}\frac{X(\ell_m,\kappa_{m'})I_{m'}(k_0)\mathscr{J}_n(\kappa_{m'}a)E_{-n,m'}(k_0,y_c)}{Q_{m'}P_m\mathscr{J}_n(\ell_m a)\sin[\sigma_{m'}(k_0)b]}
\end{aligned} \tag{43}$$

where

$$X(x_1,x_2) = \begin{cases}\dfrac{x_1\tanh x_1 H - x_2\tanh x_2 H}{x_1^2 - x_2^2} & x_1^2 \neq x_2^2\\[2ex] \dfrac{2x_1 H + \sinh 2x_1 H}{4x_1\cosh^2 x_1 H} & x_1^2 = x_2^2\end{cases}, \tag{44}$$

$\mathscr{H}_n^{(2)'}(\alpha)$ and $\mathscr{J}'_n(\alpha)$ in Eqs. (42) and (43) denote the derivatives of $\mathscr{H}_n^{(2)}(\alpha)$ and $\mathscr{J}_n(\alpha)$ with respect to α. In addition, the free edge conditions at the crack should also be imposed through $\phi^{(1)}$ and $\phi^{(2)}$. Substituting Eqs. (29) and (32) into Eqs. (7) and (8), we have

$$\begin{aligned}
&\frac{i\pi}{2}\sum_{m=-2}^{+\infty}\frac{1}{Q_m}\mathrm{B}\left[\mathscr{H}_{-n}^{(2)}(\kappa_m a)\right]a_{-n,m} + \sum_{n'=-\infty}^{+\infty}\sum_{m=-2}^{+\infty}\mathscr{C}_{n',n,m}\mathrm{B}[\mathscr{J}_n(\kappa_m a)]a_{n',m} + \sum_{n'=-\infty}^{+\infty}\sum_{m=-2}^{+\infty}\sum_{m'=-2}^{+\infty}\mathscr{D}_{n',n,m',m}\mathrm{B}[\mathscr{J}_n(\kappa_m a)]a_{n',m'}\\
&\qquad = -i\frac{\omega A}{\chi(k_0)}\sum_{m=-2}^{+\infty}\frac{I_m(k_0)E_{-n,m}(k_0,y_c)}{Q_m\sin[\sigma_m(k_0)b]}\mathrm{B}[\mathscr{J}_n(\kappa_m a)],
\end{aligned} \tag{45a}$$

$$\begin{aligned}
&\frac{i\pi}{2}\sum_{m=-2}^{+\infty}\frac{1}{Q_m}\mathrm{S}\left[\mathscr{H}_{-n}^{(2)}(\kappa_m a)\right]a_{-n,m} + \sum_{n'=-\infty}^{+\infty}\sum_{m=-2}^{+\infty}\mathscr{C}_{n',n,m}\mathrm{S}[\mathscr{J}_n(\kappa_m a)]a_{n',m} + \sum_{n'=-\infty}^{+\infty}\sum_{m=-2}^{+\infty}\sum_{m'=-2}^{+\infty}\mathscr{D}_{n',n,m',m}\mathrm{S}[\mathscr{J}_n(\kappa_m a)]a_{n',m'}\\
&\qquad = -i\frac{\omega A}{\chi(k_0)}\sum_{m=-2}^{+\infty}\frac{I_m(k_0)E_{-n,m}(k_0,y_c)}{Q_m\sin[\sigma_m(k_0)b]}\mathrm{S}[\mathscr{J}_n(\kappa_m a)].
\end{aligned} \tag{45b}$$

Substituting Eq. (33) into Eqs. (7) and (8), we have

$$\sum_{m=-2}^{+\infty}\mathrm{B}[\mathscr{J}_n(\ell_m a)]b_{n,m} = 0, \tag{46a}$$

$$\sum_{m=-2}^{+\infty} \mathrm{S}[\mathscr{J}_n(\kappa_m a)] b_{n,m} = 0, \tag{46b}$$

where

$$\mathrm{B}[\mathscr{J}_n(\kappa_m a)] = \left[\left(\kappa_m^2 - \frac{n^2 \nu_i^{'}}{a^2}\right)\mathscr{J}_n(\kappa_m a) + \frac{\nu_i^{'}}{a}\kappa_m \mathscr{J}_n^{'}(\kappa_m a)\right]\kappa_m \tanh\kappa_m H, \tag{47a}$$

$$\mathrm{S}[\mathscr{J}_n(\kappa_m a)] = \left[\left(\kappa_m^2 + \frac{n^2 \nu_i^{'}}{a^2}\right)\kappa_m \mathscr{J}_n^{'}(\kappa_m a) - \frac{n^2 \nu_i^{'}}{a^3}\mathscr{J}_n(\kappa_m a)\right]\kappa_m \tanh\kappa_m H. \tag{47b}$$

The infinite series in Eqs. (29), (32) and (33) are truncated at $n = n^{'} = \pm N$ and $m = m^{'} = M$. In such a case, there is a total number of $2(2N+1)(M+5)$ unknowns, $2(2N+1)(M+3)$ of which are $a_{n,m}$ and $b_{n,m}$, and $4(2N+1)$ of which are c_n, d_n, e_n and f_n. From Eqs. (42) and (43), $2(2N+1)(M+3)$ equations can be established, while Eqs. (45) and (46) provide additional $4(2N+1)$ equations. Thus, a total number of $2(2N+1)(M+5)$ equations can be obtained, which is the same as that of the unknowns.

When the inner and outer ice sheets have the same $L_i = L$ and $m_i = M$ $(i = 1, 2)$, the integrals on the right-hand sides of Eqs. (39) and (40) can be written in terms of the orthogonal product. From these two equations, $a_{n,m}$ and $b_{n,m}$ can be explicitly written in terms of c_n and d_n and they can be eliminated from the matrix equation. This is the same as by redefining S_I in Eq. (12) as both the inner and outer ice sheet surfaces and removing the vertical surface at $r = a$. When integration by parts is used for both ice sheet surfaces, the equation will become one involving the line integral along the crack only, and of c_n and d_n are the only unknowns.

The above formulation is derived for a crack between two ice sheets of different properties. In fact, as mentioned in the Introduction, the formulation can be used for a variety of problems. If we let $\mathscr{C}_{n,n',m} = \mathscr{D}_{n,n',m,m'} = 0$, $\phi_D^{(1)}$ in Eq. (29) becomes the diffraction velocity in the unbounded ocean. If we let $h_1 = 0$, remove $\mathscr{D}_{n,n',m,m'}$, c_n and d_n terms from Eq. (42), remove Eq. (45) and let the integration in $\mathscr{C}_{n,n',m}$ passes over the singularities at $\sigma_m \sin\sigma_m b = 0$, the problem becomes an elastic disc floating on the free surface. Similarly, when $h_2 = 0$, it becomes the problem of wave diffraction by a polynya in an ice-covered channel. Furthermore, if we remove the first term on the right-hand of Eq. (39) and corresponding $b_{n,m}$ in Eq. (42), then Eqs. (42) and (47a) become identical to those for a vertical cylinder in an ice-covered channel (Yang et al., 2022). For a non-circular shape, the vertical mode expansion can still be used, while the horizontal plane, the problem can be solved numerically.

3.3. Far-field behaviour of the solution

We may apply

$$\lim_{|x|\to+\infty} \mathrm{P.V.} \int_0^{+\infty} \frac{f(k)e^{\mathrm{i}kx}}{k - k_s} dk = \mathrm{sgn}(x)\mathrm{i}\pi f(k_s)e^{\mathrm{i}k_s x} \tag{48}$$

to Eq. (28). Noticing that the Bessel functions tend to 0, $\phi_D^{(1)}$ at $x \to \pm\infty$ can be expressed as

$$\phi_D^{(1)}(x, y, z) = \sum_{j=0}^{N_S-1} \sum_{m=-2}^{+\infty} \alpha_{j,m}^{\pm} \psi_m(z) f_{j,m}(y) e^{\mp \mathrm{i}k_j(x - x_c)}, \tag{49}$$

where

$$\alpha_{j,m}^{\pm} = \begin{cases} \dfrac{-2\pi \mathrm{i} I_m(k_j)}{Q_m \mathscr{T}_S^{'}(k_j, \omega)\tan[\sigma_m(k_j)b]} \displaystyle\sum_{n=-\infty}^{+\infty} \sum_{m'=-2}^{+\infty} \frac{a_{n,m'} I_{m'}(k_j) E_{\pm n,m'}(k_j, y_c)}{Q_{m'} \sin[\sigma_{m'}(k_j)b]} & \text{at } \mathscr{T}_S(k_j, \omega) = 0 \\ \dfrac{-2\pi \mathrm{i} I_m(k_j)}{Q_m \mathscr{T}_A^{'}(k_j, \omega)\cot[\sigma_m(k_j)b]} \displaystyle\sum_{n=-\infty}^{+\infty} \sum_{m'=-2}^{+\infty} \frac{a_{n,m'} I_{m'}(k_j) F_{\pm n,m'}(k_j, y_c)}{Q_{m'} \cos[\sigma_{m'}(k_j)b]} & \text{at } \mathscr{T}_A(k_j, \omega) = 0 \end{cases}, \tag{50}$$

$$f_{j,m}(y) = \begin{cases} \dfrac{\cos[\sigma_m(k_j)y]}{\cos[\sigma_m(k_j)b]} & \text{at } \mathscr{T}_S(k_j, \omega) = 0 \\ \dfrac{\sin[\sigma_m(k_j)y]}{\sin[\sigma_m(k_j)b]} & \text{at } \mathscr{T}_A(k_j, \omega) = 0 \end{cases}, \tag{51}$$

$\mathscr{T}_S^{'}(k, \omega)$ and $\mathscr{T}_A^{'}(k, \omega)$ respectively denote the derivatives of $\mathscr{T}_S(k, \omega)$ and $\mathscr{T}_A(k, \omega)$ with respective to k. Using Eqs. (10) and (49), we have

$$\phi = \begin{cases} \sum_{m=-2}^{+\infty} \mathscr{P}_m \psi_m(z)\, f_{0,m}(y) e^{-\mathrm{i}k_0(x-x_c)} + \sum_{j=0}^{N_S-1} \sum_{m=-2}^{+\infty} \mathscr{R}_{j,m} \psi_m(z) f_{j,m}(y) e^{\mathrm{i}k_j(x-x_c)} & x = -\infty \\ \sum_{j=0}^{N_S-1} \sum_{m=-2}^{+\infty} \mathscr{T}_{j,m} \psi_m(z) f_{j,m}(y) e^{-\mathrm{i}k_j(x-x_c)} & x = +\infty \end{cases}, \tag{52}$$

where $\mathscr{R}_{j,m} = \alpha_{j,m}^{-}$ and $\mathscr{T}_{j,m} = \alpha_{j,m}^{+} + \delta_{j,0}\mathscr{P}_m$, and

$$\mathscr{P}_m = \mathrm{i}\frac{\omega A}{\chi(k_0)} \frac{I_m(k_0)}{Q_m \tan[\sigma_m(k_0)b]}. \tag{53}$$

Notice $\overline{\psi}_m(z) = \psi_m(z)$, $\overline{f}_{j,m}(y) = f_{j,m}(y)$ when $m \geq 0$, as well as $\overline{\psi} - 1(z) = \psi_{-2}(z)$, $\overline{\psi}_{-2}(z) = \psi_{-1}(z)$, $\overline{f}_{j,-1}(y) = f_{j,-2}(y)$, $\overline{f}_{j,-2}(y) = f_{j,-1}(y)$, $\overline{\mathscr{P}}_{-1} = \mathscr{P}_{-2}$, $\overline{\mathscr{P}}_{-2} = \mathscr{P}_{-1}$ since $\kappa_{-2} = -\overline{\kappa}_{-1}$ and $\sigma_{-2}(k_j) = -\overline{\sigma}_{-1}(k_j)$. $\overline{\phi}$ then can be expressed as

$$\overline{\phi} = \begin{cases} \sum_{m=-2}^{+\infty} \widetilde{\mathscr{P}}_m \psi_m(z)\, f_{0,m}(y) e^{-\mathrm{i}k_0(x-x_c)} + \sum_{j=0}^{N_S-1} \sum_{m=-2}^{+\infty} \widetilde{\mathscr{R}}_{j,m} \psi_m(z) f_{j,m}(y) e^{-\mathrm{i}k_j(x-x_c)} & x = -\infty \\ \sum_{j=0}^{N_S-1} \sum_{m=-2}^{+\infty} \widetilde{\mathscr{T}}_{j,m} \psi_m(z) f_{j,m}(y) e^{\mathrm{i}k_j(x-x_c)} & x = +\infty \end{cases}. \tag{54}$$

where

$$\widetilde{\mathscr{P}}_m = \begin{cases} \overline{\mathscr{P}}_{-1} & m = -2 \\ \overline{\mathscr{P}}_{-2} & m = -1 \\ \overline{\mathscr{P}}_m & m \geq 0 \end{cases}, \tag{55}$$

and $\widetilde{\mathscr{R}}_{j,m}$, $\widetilde{\mathscr{T}}_{j,m}$ $\widetilde{\mathscr{R}}_{j,m}$, $\widetilde{\mathscr{T}}_{j,m}$ are defined in the same way. Substituting Eqs. (52) and (54) into Eq. (B3) and using Eq. (B5), we obtain

$$I_+(x) = \int_{-b}^{b} \left[\left\langle \phi, \frac{\partial \overline{\phi}}{\partial x} \right\rangle - \left\langle \overline{\phi}, \frac{\partial \phi}{\partial x} \right\rangle \right]_{x=+\infty} dy = \mathrm{i} \sum_{j=0}^{N_S-1} \sum_{l=0}^{N_S-1} \sum_{m=-2}^{+\infty} Q_m \mathscr{T}_{j,m} \widetilde{\mathscr{T}}_{l,m}(k_j + k_l) e^{\mathrm{i}(k_l - k_j)(x-x_c)} \int_{-b}^{b} f_{j,m}(y) f_{l,m}(y) dy. \tag{56}$$

Invoking Eq. (B8), $I_+(x)$ is independent to x, Eq. (56) can be simplified as

$$I_+ = 2\mathrm{i} \sum_{j=0}^{N_S-1} \sum_{m=-2}^{+\infty} k_j Q_m \mathscr{T}_{j,m} \widetilde{\mathscr{T}}_{j,m} Y(\sigma_m(k_j)), \tag{57}$$

where

$$Y(\sigma_m(k_j)) = \begin{cases} \dfrac{2\sigma_m(k_j)b + \sin[2\sigma_m(k_j)b]}{2\sigma_m(k_j)\cos^2[\sigma_m(k_j)b]} & \text{at } \mathscr{T}_S(k_j, \omega) = 0 \\ \dfrac{2\sigma_m(k_j)b - \sin[2\sigma_m(k_j)b]}{2\sigma_m(k_j)\sin^2[\sigma_m(k_j)b]} & \text{at } \mathscr{T}_A(k_j, \omega) = 0 \end{cases}. \tag{58}$$

The integral at $x = -\infty$ in Eq. (B4) can be treated in the same way, which provides

$$I_- = -2\mathrm{i} \sum_{j=0}^{N_S-1} \sum_{m=-2}^{+\infty} k_j Q_m \mathscr{R}_{j,m} \widetilde{\mathscr{R}}_{j,m} Y(\sigma_m(k_j)) + 2\mathrm{i} \sum_{m=-2}^{+\infty} k_0 Q_m \mathscr{P}_m \widetilde{\mathscr{P}}_m Y(\sigma_m(k_0)). \tag{59}$$

From Eqs. (B3), (57) and (59), we have

$$\sum_{j=0}^{N_S-1} \left(U_j^T + U_j^R \right) = U_I, \tag{60}$$

where

$$\begin{cases} U_j^T = k_j \sum_{m=-2}^{+\infty} Q_m \mathscr{T}_{j,m} \widetilde{\mathscr{T}}_{j,m} Y(\sigma_m(k_j)) \\ U_j^R = k_j \sum_{m=-2}^{+\infty} Q_m \mathscr{R}_{j,m} \widetilde{\mathscr{R}}_{j,m} Y(\sigma_m(k_j)) \\ U_I = k_0 \sum_{m=-2}^{+\infty} Q_m \mathscr{P}_m \widetilde{\mathscr{P}}_m Y(\sigma_m(k_0)) \end{cases}, \tag{61a, b, c}$$

U_j^T and U_j^R denote a measure of the energy of the k_j component of the transmitted and reflected waves respectively, U_I represents a measure of the energy of the incident wave. For convenience, the transmission and reflection coefficients of the wave components k_j can be defined as

$$T_j = \left(\frac{U_j^T}{U_I}\right)^{1/2} \text{ and } R_j = \left(\frac{U_j^R}{U_I}\right)^{1/2} \tag{62a, b}$$

Thus, from Eqs. (60) and (62), T_j and R_j satisfy

$$\sum_{j=0}^{N_S-1} \left(T_j^2 + R_j^2\right) = 1. \tag{63}$$

3.4. Hydrodynamic forces on the inner circular ice sheet

Once the velocity potential $\phi^{(2)}$ is found, the hydrodynamic forces on the inner circular ice sheet can be calculated through

$$F_j = \mathrm{i}\omega\rho \iint_{S_{I2}} \phi^{(2)} n_j dS,\ j = 1,\ 2,\ 3. \tag{64}$$

where $j = 1$ corresponds to the vertical force F_z, and $j = 2$ and 3 correspond to the moment M_x about the line $x = x_c$ & $z = 0$ and the moment M_y about the line $y = y_c$ & $z = 0$, and $(n_1, n_2, n_3) = (1, y - y_c, x_c - x) = (1, r\sin\theta, -r\cos\theta)$. Substituting Eq. (33) into (64), and using (Abramowitz and Stegun, 1965)

$$\int_0^z t^n \mathscr{J}_{n-1}(t) dt = z^n \mathscr{J}_n(z), \tag{65}$$

we obtain

$$\begin{bmatrix} F_z \\ M_x \\ M_y \end{bmatrix} = \pi\rho\omega a \mathrm{i} \sum_{m=-2}^{+\infty} \frac{1}{\kappa_m} \times \begin{bmatrix} 2b_{0,m}\mathscr{J}_1(\kappa_m a) \\ \mathrm{i}a(b_{-1,m} + b_{1,m})\mathscr{J}_2(\kappa_m a) \\ a(b_{-1,m} - b_{1,m})\mathscr{J}_2(\kappa_m a) \end{bmatrix}. \tag{66}$$

4. Numerical results

In the cases studied below, the typical values of the physical parameters of the ice sheet and the fluid are chosen as follows:

$$\left.\begin{array}{c} \rho_1 = \rho_2 = 917\ \mathrm{kgm^{-3}},\ E_1 = E_2 = 4.2 \times 10^9\ \mathrm{Nm^{-2}},\ \nu_1 = \nu_2 = 0.3 \\ \rho = 1000\ \mathrm{kgm^{-3}},\ g = 9.8\ \mathrm{ms^{-2}},\ H = 5\ \mathrm{m} \end{array}\right\}, \tag{67}$$

unless otherwise specified. All the numerical results are presented in the dimensionless form, based on the density of water ρ, the acceleration due to gravity g, and a characteristic length scale. They are obtained by truncating the infinite series in Eqs. (42), (43), (45) and (46) at $N = 12$ and $M = 48$, which have been confirmed to be convergent.

4.1. Analysis of the distribution of the roots of the dispersion equations

Here, we may investigate further the distribution of the roots. Take the dispersion equation of the ice-covered channel with clamped – clamped edges as an example. From the derivations in Yang et al. (2022), Eq. (A3) can also be written in the following form

$$\left.\begin{aligned}\mathscr{T}_S(k,\omega) &= -2\sum_{m=-2}^{+\infty}\frac{\kappa_m^2\tanh^2\kappa_m H}{Q_m}\frac{1}{\sigma_m\tan\sigma_m b}=\frac{4\rho\omega^2}{b}\sum_{n=0}^{+\infty}\frac{\alpha_{2n}\sinh\alpha_{2n}H}{K_1(\alpha_{2n},\omega)(1+\delta_{n0})}\\ \mathscr{T}_A(k,\omega) &= 2\sum_{m=-2}^{+\infty}\frac{\kappa_m^2\tanh^2\kappa_m H}{Q_m}\frac{1}{\sigma_m\cot\sigma_m b}=\frac{4\rho\omega^2}{b}\sum_{n=0}^{+\infty}\frac{\alpha_{2n+1}\sinh\alpha_{2n+1}H}{K_1(\alpha_{2n+1},\omega)}\end{aligned}\right\},\tag{68a,b}$$

where $\alpha_n=\sqrt{k^2+n^2\pi^2/4b^2}$, and Q_m and $K_1(\alpha,\ \omega)$ are defined in Eqs. (A3) and (A7) respectively. $K_1(\alpha,\omega)$ is the dispersion equation of unbounded fluid domain with an ice-cover. It has been known that $K_1(\alpha,\omega)=0$ has only one real root at $\alpha=\kappa_0$, or $K_1(\alpha,\omega)<0$ when $\alpha<\kappa_0$ and $K_1(\alpha,\omega)>0$ when $\alpha>\kappa_0$. When $k>\kappa_0$, we have $\alpha_n>\kappa_0$, and $K_1(\alpha_n,\omega)>0$ in Eq. (68) for all n, which gives $\mathscr{T}_S(k,\omega)>0$ and $\mathscr{T}_A(k,\omega)>0$. Thus, all the positive real roots of $\mathscr{T}_S(k,\omega)$ and $\mathscr{T}_A(k,\omega)$ are located within the range of $0<k<\kappa_0$. We may denote $\lambda_j=\sqrt{\kappa_0^2-j^2\pi^2/4b^2}$, $j=0\ldots N'$, where $N'=\left[\frac{2\kappa_0 b}{\pi}\right]$, $[x]$ is the floor function. Letting $k=\lambda_{2j+2}+\epsilon$ with $\epsilon\to0^+$ and $2j+2<N'$, we have $K_1(\alpha_{2j+2},\omega)\to0^+$ and therefore $\mathscr{T}_S(k,\omega)\to+\infty$. Letting $k=\lambda_{2j}-\epsilon$, we have $K_1(\alpha_{2j},\omega)\to0^-$ and therefore $\mathscr{T}_S(k,\omega)\to-\infty$. Since $\mathscr{T}_S(k,\omega)$ is continuous in $k\in(\lambda_{2j+2},\lambda_{2j})$, there will be at least one root of $\mathscr{T}_S(k,\omega)=0$ in $k\in(\lambda_{2j+2},\lambda_{2j})$. We also notice that $\frac{k\sinh kH}{K_1(k,\omega)}$ is a decreasing function, apart from a jump from $-\infty$ at $k=\kappa_0+0^-$ to $+\infty$ at $k=\kappa_0+0^+$. Thus $\mathscr{T}_S(k,\omega)$ is a decreasing function in $k\in(\lambda_{2j+2},\lambda_{2j})$ and $\mathscr{T}_S(k,\omega)$ will have only one root k_{2j} within this range. Similarly, in $k\in(\lambda_{2j+1},\lambda_{2j-1})$, there will be one root k_{2j-1} of $\mathscr{T}_A(k,\omega)=0$. Attention should be paid when $2j<N'$ but $2j+2>N'$. In the range of $(0,\lambda_{2j})$, as $\mathscr{T}_S(k,\omega)$ is a decreasing function and $\mathscr{T}_S(k,\omega)\to-\infty$ at $k=\lambda_{2j}-\epsilon$, $\mathscr{T}_S(k,\omega)=0$ has a solution only if $\mathscr{T}_S(0,\omega)\geq0$. Noticing that $\mathscr{T}_S(0,\omega)=0$ corresponds to the natural frequency $\omega_{2j}^{(c)}$ of the channel (Yang et al., 2022), which means that only when κ_0 has passed this natural frequency, $\mathscr{T}_S(k,\omega)=0$ will have a solution in the range of $(0,\lambda_{2j})$. Besides, when $n>j+1$, all the terms in the summation of $\mathscr{T}_S(k,\omega)$ in Eq. (68a) will be positive, and the summation tends to $+\infty$ when $h_i\to0^+$. Also, as there will be a root $k_{2j}\in(\lambda_{2j+2},\ \lambda_{2j})$ of $\mathscr{T}_S(k,\omega)=0$ ($2j+2<N'$), it suggests that $k_{2j}\to\lambda_{2j}+0^-$, where $\frac{1}{K_1(\alpha_{2j},\omega)}\to-\infty$, or the root of $\mathscr{T}_S(k,\omega)=0$ will be $k_{2j}\to\lambda_{2j}$, which is consistent with the free surface problem. Furthermore, because N' increases as b increases, for a given ω, the number of real positive roots of $\mathscr{T}_S(k,\omega)=0$ and $\mathscr{T}_A(k,\omega)=0$ increases as b increases. For a finite value of j, $\lambda_{2j-1},\ \lambda_{2j},\ \lambda_{2j+1},\ \lambda_{2j+2}\to\kappa_0$ as $b\to+\infty$, which indicates that the corresponding roots of $\mathscr{T}_S(k,\omega)=0$ in $(\lambda_{2j+2},\lambda_{2j})$ and of $\mathscr{T}_A(k,\omega)=0$ in $(\lambda_{2j+1},\lambda_{2j-1})$ all tend to κ_0.

4.2. Two identical ice sheets separated by a circular crack

At the edge of the circular crack, there will be jumps of the displacement and slope, which can be written as

$$\widehat{\eta}(\theta)=\frac{1}{\mathrm{i}\omega}\frac{\partial\left[\phi^{(1)}(a,\theta,0)-\phi^{(2)}(a,\theta,0)\right]}{\partial z}\ \text{and}\ \widehat{\eta}_r(\theta)=\frac{1}{\mathrm{i}\omega}\frac{\partial^2\left[\phi^{(1)}(a,\theta,0)-\phi^{(2)}(a,\theta,0)\right]}{\partial r\partial z},\tag{69a,b}$$

Invoking Eqs. (29), (32), (33) and (41), we have

$$\widehat{\eta}(\theta)=\sum_{n=-\infty}^{+\infty}\varkappa_n e^{\mathrm{i}n\theta}\ \text{ and }\ \widehat{\eta}_r(\theta)=\sum_{n=-\infty}^{+\infty}\vartheta_n e^{\mathrm{i}n\theta}.\tag{70a,b}$$

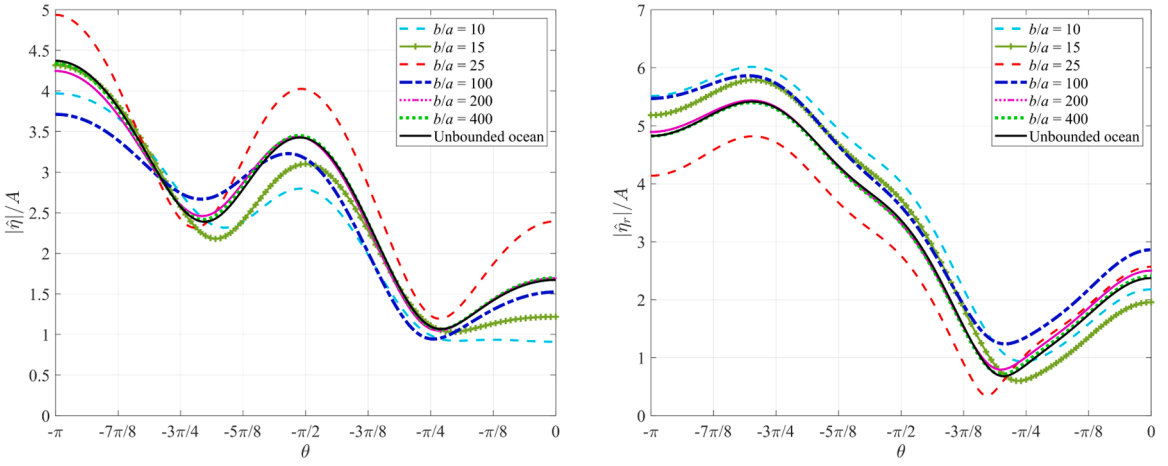

Fig. 2. Jumps of displacement and slope across the crack under different channel widths (free – free on channel walls). The circular crack is at the centre of the channel $\left(y_c=0,\frac{h_1}{a}=\frac{h_2}{a}=0.0\right)5$.

where

$$w_n = \frac{1}{\mathrm{i}\omega}\left\{\begin{array}{l} \dfrac{\mathrm{i}\pi}{2}\displaystyle\sum_{m=-2}^{+\infty}\frac{a_{-n,m}\mathscr{H}^{(2)}_{-n}(\kappa_m a)\kappa_m \tanh\kappa_m H}{Q_m} \\ \quad + \displaystyle\sum_{n'=-\infty}^{+\infty}\sum_{m=-2}^{+\infty} a_{n',m}\mathscr{C}_{n',n,m}\mathscr{J}_n(\kappa_m a)\kappa_m \tanh\kappa_m H \\ \quad + \displaystyle\sum_{n'=-\infty}^{+\infty}\sum_{m=-2}^{+\infty}\sum_{m'=-2}^{+\infty} a_{n',m}\mathscr{D}_{n',n,m,m'}\mathscr{J}_n(\kappa_{m'} a)\kappa_{m'} \tanh\kappa_{m'} H \\ \quad + \dfrac{\mathrm{i}\omega A}{\chi(k_0)}\displaystyle\sum_{m=-2}^{+\infty}\frac{I_m(k_0)E_{-n,m}(k_0,y_c)\mathscr{J}_n(\kappa_m a)\kappa_m \tanh\kappa_m H}{Q_m \sin[\sigma_m(k_0)b]} + e_n \end{array}\right\}, \tag{71a}$$

$$\vartheta_n = -\frac{1}{\mathrm{i}\omega}\left\{c_n + \sum_{m=-2}^{+\infty} b_{n,m}\mathscr{J}'_n(\mathscr{k}_m a)\mathscr{k}_m^2 \tanh\mathscr{k}_m H\right\}. \tag{71b}$$

The numerical results of $|\widehat{\eta}(\theta)|$ and $|\widehat{\eta}_r(\theta)|$ are given in Fig. 2 with $H/a = 5$. The physical parameters here are chosen to be the same as those in Fig. 2 in Li et al. (2018). It can be seen that when at $b/a = 10$ and effect of channel width is highly significant. This seems to be very much different from the free surface channel problem. There for the wave radiation and diffraction problem of a sphere (Wu, 1998a) and the wave-making resistance problem of a sphere (Wu, 1998b), the channel wall effect becomes insignificant when $b/a \approx 10$, apart from near natural frequencies of the channel in the radiation and diffraction problem. Here from $b/a = 10$ to $b/a = 200$, there is a big change in the results. When $b/a > 200$, the effect of the channel wall begins to diminish and at $b/a = 400$, the result is almost identical to that in the unbounded ocean (Li et al., 2018).

We may then consider the hydrodynamic forces on the inner circular ice sheet at different values of channel widths. The numerical results for $|F_z|$ and $|M_y|$ versus $\kappa_0 a$ with clamped – clamped and free – free edges channel wall conditions are given in Figs. 3 and 4 respectively. It can be seen from Figs. 3(a) and 4(a) that while the main trend of the curves of $|F_z|$ follows that in unbounded ocean, a series of rapid changes can be observed in the curves of $|F_z|$ when $\kappa_0 a$ is close to one of the natural frequencies of the ice-covered channel. It should be noted that as the problem is symmetric about $y = 0$, only those natural frequencies corresponding to $\mathscr{T}_S(k,\omega) = 0$ have an impact, which are given in Table 1. Different from $|F_z|$, in Figs. 3(b) and 4(b), the rapid changes are not observed in the curves of $|M_y|$ versus $\kappa_0 a$. The reason for the different behaviours between $|F_z|$ and $|M_y|$ is actually similar to that discussed in (Yang et al., 2022) about the horizontal forces and shear forces on a vertical cylinder. From Eq. (66), it can be known that F_z is related to $b_{0,m}$, while M_y is related to $b_{\pm1,m}$. Since the present case is symmetric about $y = 0$, it can be found from Eq. (33) that $b_{n,m} = (-1)^n b_{-n,m}$, and Eq. (37) can be further simplified as

$$\phi^{(2)}(r,\theta,z) = 2\sum_{n=0}^{+\infty}\left(\frac{1}{1+\delta_{n0}}\right)\times b_{n,m}\mathscr{J}_n(\mathscr{k}_m r)\varphi_m(z)\cos n\theta. \tag{72}$$

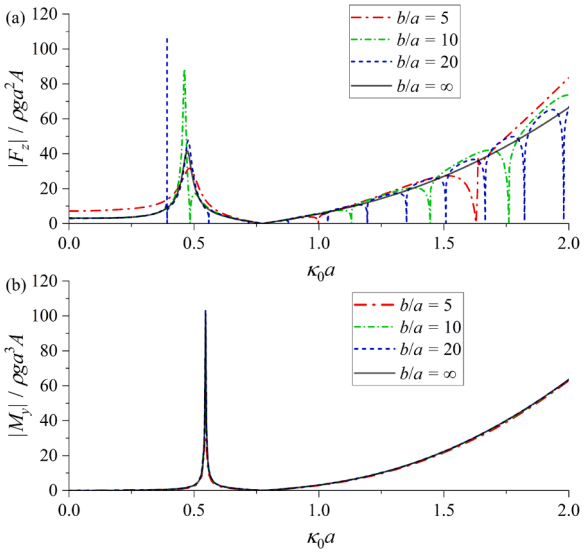

Fig. 3. Force and moment on the inner ice sheet (clamped – clamped on channel walls, $\frac{H}{a} = 5, h_{1\bar{a}} = \frac{h_2}{a} = 0.1, y_c/a = 0$). (a) F_z; (b) M_y.

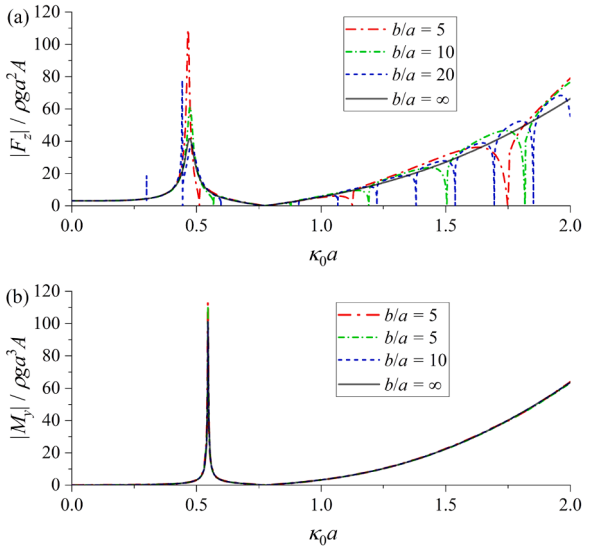

Fig. 4. Force and moment on the inner ice sheet (free – free on channel walls, $H/a = 5$, $h_1/a = h_2/a = 0.1$, $y_c/a = 0$). (a) F_z; (b) M_y.

Table 1
Natural frequencies of the symmetric modes ($\mathscr{T}_S(k,\omega) = 0$) with clamped- clamped edges on the channel walls ($H/a = 5$, $h_1/a = 0.1$).

j	$b/a = 5$			$b/a = 10$			$b/a = 20$		
	$\omega_c^{(2j)}\sqrt{\frac{a}{g}}$	$\kappa_0 a$	$\frac{\kappa_0 b}{\pi}$	$\omega_c^{(2j)}\sqrt{\frac{a}{g}}$	$\kappa_0 a$	$\frac{\kappa_0 b}{\pi}$	$\omega_c^{(2j)}\sqrt{\frac{a}{g}}$	$\kappa_0 a$	$\frac{\kappa_0 b}{\pi}$
1	6.0332	0.9976	1.5877	1.2005	0.4842	1.5414	0.3977	0.1989	1.2665
2	20.0193	1.6358	2.6035	3.7065	0.8133	2.5888	0.8388	0.3924	2.4983
3	44.1697	2.2683	3.6102	8.1687	1.1309	3.5997	1.5995	0.5595	3.5617
4	79.6859	2.9000	4.6148	14.8518	1.4466	4.6047	2.7884	0.7199	4.5829
5	127.4431	3.5302	5.6185	23.9680	1.7618	5.6080	4.4485	0.8785	5.5925

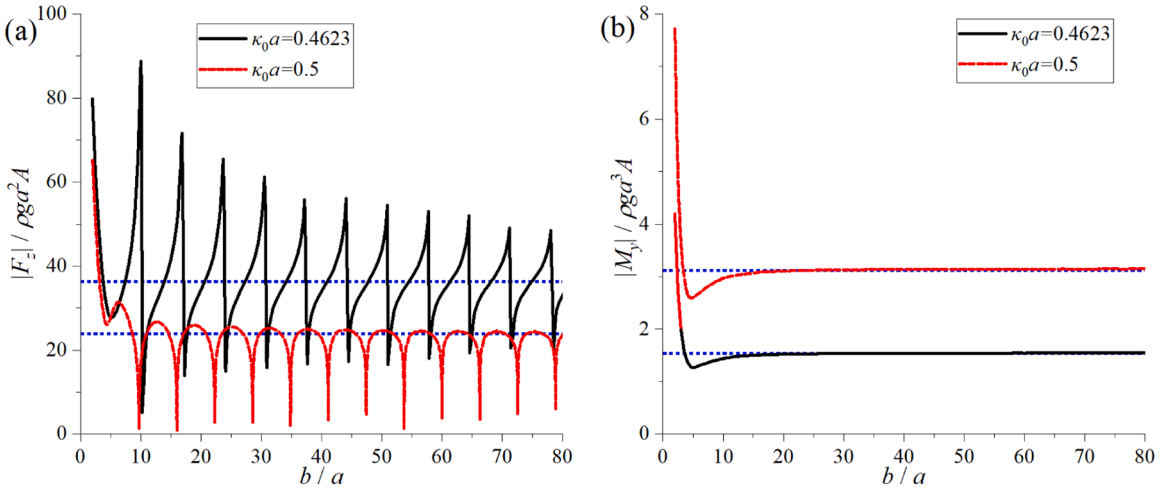

Fig. 5. Force and moment on the inner ice sheet versus the channel width at two different wave numbers (clamped – clamped on channel walls, $H/a = 5$, $h_1/a = h_2/a = 0.1$, $y_c/a = 0$). (a) F_z; (b) M_y. The blue dot lines correspond to the values in the unbounded ocean.

As explained in Yang et al. (2022), the system of linear equations for $a_{n,m}$, $b_{n,m}$, $c_n \sim f_n$ (n is odd) here is in fact independent to that of $a_{n,m}$, $b_{n,m}$, $c_n \sim f_n$ (n is even). For even n, the coefficient $\mathscr{D}_{n,n',m,m'}$ will be singular at these natural frequencies, but for odd n, $\mathscr{D}_{n,n',m,m'}$ will be bounded. In such a case, the behaviours of $|F_z|$ and $|M_y|$ near the natural frequencies cannot be expected to be the same. Away from the natural frequencies, both $|F_z|$ and $|M_y|$ are much closer to those in the unbounded ocean. In fact, even at $b/a = 5$, they are not too

much different from those in the unbounded ocean. Compared with Fig. 2, one can therefore see that while the impact of channel width on the ice sheet deflection near the crack is highly significant, the effect on the force is much smaller, as in the free surface problem. For this reason, the edge conditions on the channel wall have a much smaller effect on $|F_z|$ but $|M_y|$, as can be observed in Figs. 3 and 4.

In Figs. 3 and 4, away from natural frequencies, an additional peak can be obviously observed. In Fig. 3, from the curves of $b/a = 5$, 10, 20 and ∞, there are peaks at $\kappa_0 a = 0.4841$, 0.4623, 0.4763 and 0.4751 for $|F_z|$, as well as $\kappa_0 a = 0.5457$, 0.5461, 0.5461 and 0.5461 for $|M_y|$. As discussed in Li et al. (2018) for the case $b/a = \infty$, these peaks are in fact related to the natural frequency of the motion of the inner ice sheet. Mathematically, the frequency at which the determinant of the matrix corresponding to the system of linear equations for $a_{n,m}$, $b_{n,m}$ and $c_n \sim f_n$ is 0 will be a complex, because the system has the damping effect due to wave radiation. When ω is real, the determinant of the matrix will not be zero. However, the determinant can be very small when ω is close to the complex natural frequency or at the undamped motion natural frequency, which makes some of the coefficients in $a_{n,m}$ and $b_{n,m}$ very large. In particular, $b_{0,m}$ is very large when $\kappa_0 a = 0.4841$, 0.4623, 0.4763 and 0.4751, $b_{\pm 1,m}$ is very large when $\kappa_0 a = 0.5457$, 0.5461, 0.5461 and 0.5461 corresponding to $b/a = 5$, 10, 20 and ∞. This explains the behaviour of $|F_z|$ and $|M_y|$ at these points. It can be also observed these values of undamped motion natural frequencies are not very sensitive to the channel widths and edge conditions, but the corresponding peak values of $|F_z|$ and $|M_y|$ are significantly affected.

We may further show how the force and moment on the inner ice sheet vary with the half channel width b. In Fig. 5 (a), at $\kappa_0 a = 0.5$, with the increase of b/a, $|F_z|$ gradually approaches the value of the unbounded ocean when $\kappa_0 a$ is not near the natural frequencies of the channel. When $\kappa_0 a$ is near one of the natural frequencies, $|F_z|$ drops significantly and it then returns to the original trajectory towards the blue dotted line corresponding to the unbounded ocean. At $\kappa_0 a = 0.4623$, which is near the natural frequency of the motion of the inner ice sheet when $b/a = 10$, as seen in Fig. 3 (a). Although the result also tends to that in the unbounded ocean, shown in the blue dotted line, its curve oscillates around the dotted line, and it approaches the dotted line more slowly than the case of $\kappa_0 a = 0.5$. Thus, the way at which the result tends to that in the unbounded ocean is very different at different frequencies. In Fig. 5 (b), at both frequencies, the moment $|M_y|$ shows some differences with that in the unbounded ocean only when b/a is small. When $b/a > 20$, the effect of the channel walls has almost diminished. This is consistent with what has been observed in Figs. 3 (b) and 4 (b).

The deflection $\eta^{(i)}$ $(i = 1, 2)$ of the inner and outer ice sheets are also considered. The deflection at the centre of the inner ice sheet versus the half channel width b is presented in Fig. 6. It can be found that $|\eta^{(2)}|$ shows a quite similar behaviour with $|F_z|$ given in Fig. 5 (a). We further show the behaviour of the wave profile when $\kappa_0 a$ near one of the channel's natural frequencies $\kappa_0 a \approx 0.4842$ at $b/a = 10$. Fig. 7 gives results at two frequencies, $\kappa_0 a = 0.484$ and $\kappa_0 a = 0.485$, which are respectively just below and just above the natural frequency. These two frequencies are very close, but a significant difference can be observed in Figs. 7 (a) and (b), which indicates that ice sheet deflection also experiences a rapid change near one of the natural frequencies of the channel. Furthermore, the ice sheet deflection at $\kappa_0 = 0.546$ and $\kappa_0 a = 0.547$ at $b/a = 10$ are given in Fig. 8, which are close to the undamped motion natural frequency $\kappa_0 a \approx 0.5461$ of the inner ice sheet. It can be seen that the deflection of the inner sheet is very large and can be well over 100 times the incoming wave amplitude. This clearly shows that the inner sheet is near resonance. It can also be seen from Fig. 8 that the deflection of the outer ice sheet is much smaller. This is because two ice sheets are fully disconnected at the crack. Their interactions are through waves, not through the shear force and moment at the crack.

Apart from the hydrodynamic forces on the inner circular ice sheet and the ice sheet deflection, we may also consider the energy of the transmitted and reflected waves at infinity. From Eq. (60), we may define

$$U^T = \frac{\sum_{j=0}^{N_S-1} U_j^T}{U_I} \text{ and } U^R = \frac{\sum_{j=0}^{N_S-1} U_j^R}{U_I} \tag{73}$$

as a measure of the wave energy at $x = \pm\infty$. An example of U^T and U^R versus $\kappa_0 a$ at different channel widths are given in Fig. 9. It can be observed that U^T is normally larger than U^R in these three cases. However, at $b/a = 5$ and $b/a = 10$, when $\kappa_0 a$ is near one of the undamped motion natural frequencies discussed above, sudden changes on U^T and U^R leads to $U^T < U^R$, and even $U^T \to 0$ and $U^R \to 1$ at

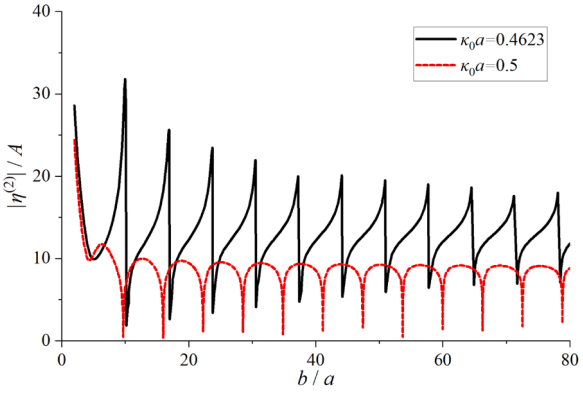

Fig. 6. The deflection at the centre position of the inner ice sheet versus the channel width at two different wave numbers (clamped – clamped on channel walls, $H/a = 5$, $h_1/a = h_2/a = 0.1$, $y_c/a = 0$).

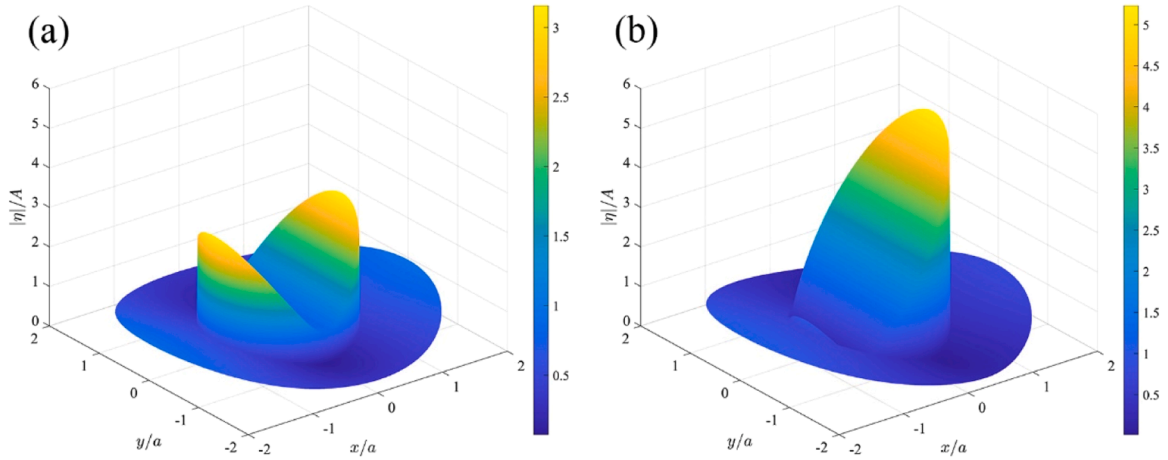

Fig. 7. The modulus of the ice sheet deflection (clamped – clamped on channel walls, $b/a = 10$, $H/a = 5$, $h_1/a = h_2/a = 0.1$, $y_c/a = 0$). (a) $\kappa_0 a = 0.484$; (b) $\kappa_0 a = 0.485$.

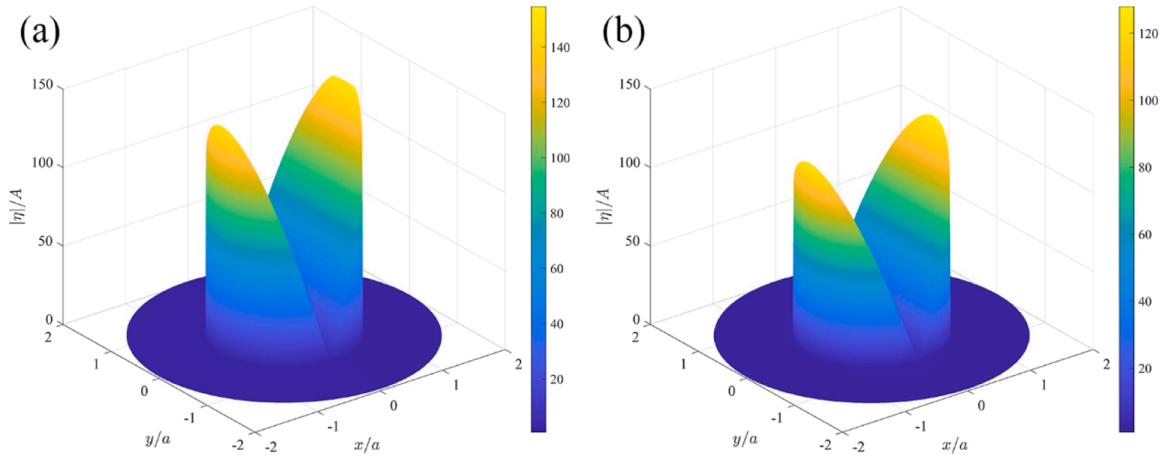

Fig. 8. The modulus of the ice sheet deflection (clamped – clamped on channel walls, $b/a = 10$, $H/a = 5$, $h_1/a = h_2/a = 0.1$, $y_c/a = 0$). (a) $\kappa_0 a = 0.546$; (b) $\kappa_0 a = 0.547$.

some value of $\kappa_0 a$. By contrast, the sudden changes on U^T and U^R occurred when $\kappa_0 a$ is near one of the channel's natural frequencies are not so drastic. Besides, when $\kappa_0 a$ is away from these natural frequencies, as b/a increases the value of U^T gradually increases and U^R gradually decreases

To show how the energy of each k_j wave component varies at infinity, the transmission and reflection coefficients of the first five components at $b/a = 10$ are given in Fig. 10. Initially, at small $\kappa_0 a$, there is only one wave component k_0 at infinity. As discussed below Eq. (68), when κ_0 has passed a value corresponding to each natural frequency $\omega_{2j}^{(c)}$, a new symmetric wave component k_{2j} will appear. At the natural frequency $\omega = \omega_{2j}^{(c)}$ $(j = 1, 2, \ldots)$ and, $k_{2j} = 0$, sudden changes of T_{2j} and R_{2j} can be observed. It can be seen that T_0 is normally the most significant component over the most ranges of $\kappa_0 a$, which means the transmitted energy at $x = +\infty$ is normally dominated by the k_0 component. It can also be seen that when $\kappa_0 a$ passes the value corresponding to the natural frequency $\omega_{2j}^{(c)}$, R_{2j} will be the main component of the reflection coefficients in a small range close to the natural frequency. This means that R_0 is not always the largest one.

Computations are also conducted for a circular crack at off-centre positions of the channel. The hydrodynamic forces on the inner ice sheet are given in Fig. 11. Because the problem is asymmetric, M_x is no longer zero and its results are provided in Fig. 11 (b). In this case the natural frequencies corresponding to both the symmetrical mode $\mathscr{T}_S(k, \omega) = 0$ and the anti-symmetric modes $\mathscr{T}_A(k, \omega) = 0$ will have effects. Thus, there are more oscillations on $|F_z|$ and $|M_x|$ curves when $y_c/a \neq 0$. However, the curve of $|M_y|$ still remains smooth. In fact, $\phi^{(2)}$ in Eq. (33) can be further written as

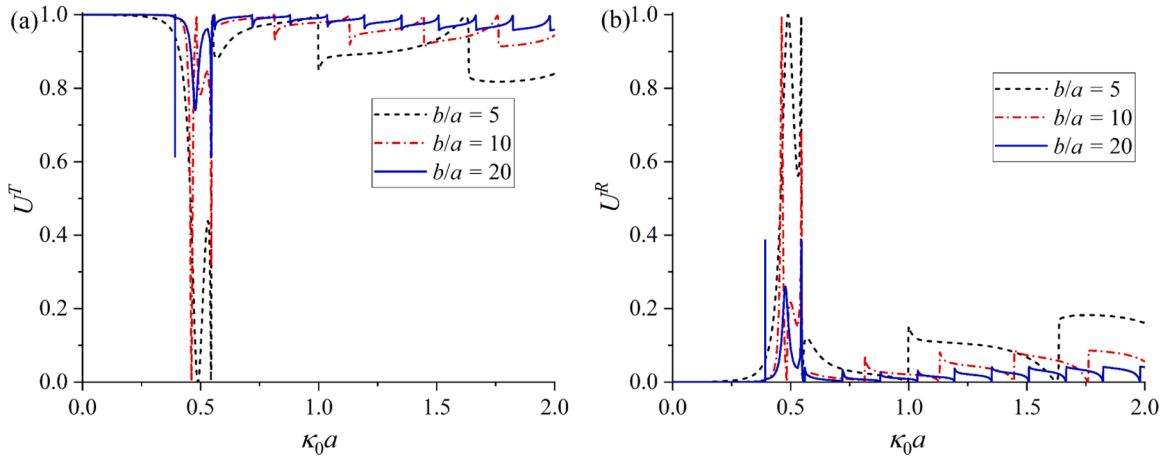

Fig. 9. The wave transmission and reflection coefficients at infinity (clamped – clamped on channel walls, $H/a = 5$, $h_1/a = h_2/a = 0.1$, $y_c/a = 0$) (a) U^T; (b) U^R.

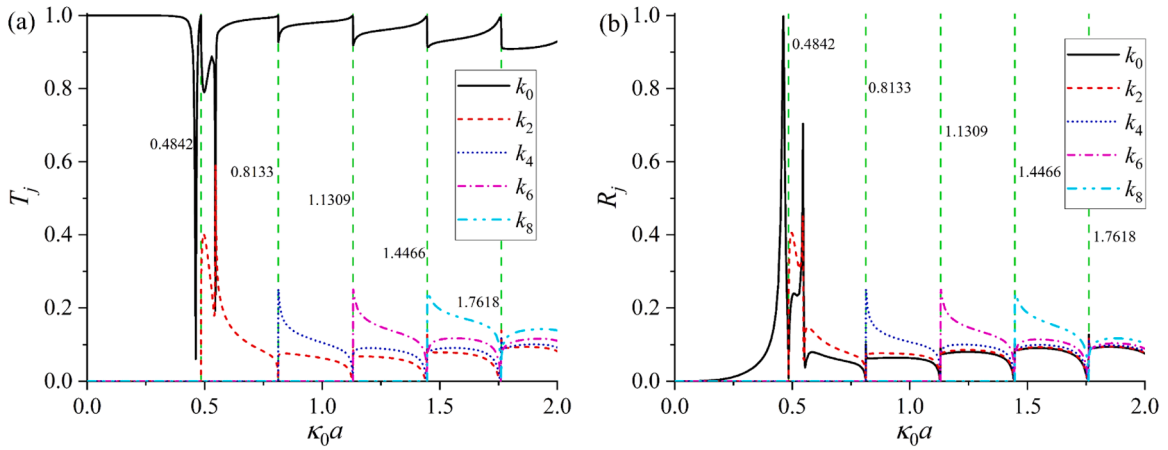

Fig. 10. The transmission and reflection coefficients of each wave component (clamped – clamped on channel walls, $b/a = 10$, $H/a = 5$, $h_1/a = h_2/a = 0.1$, $y_c/a = 0$). (a) T_j; (b) R_j.

$$\phi^{(2)}(r,\theta,z) = \sum_{n=0}^{+\infty}\sum_{m=-2}^{+\infty}\left\{\left[\frac{b_{n,m}+(-1)^n b_{-n,m}}{1+\delta_{n0}}\right]\cos n\theta + \mathrm{i}\left[\frac{b_{n,m}-(-1)^n b_{-n,m}}{1+\delta_{n0}}\right]\sin n\theta\right\}\mathscr{J}_n(\kappa_m r)\varphi_m(z). \tag{74}$$

If we define $\frac{b_{n,m}+(-1)^n b_{-n,m}}{1+\delta_{n0}} = f_{n,m}$, $\mathrm{i}\frac{b_{n,m}-(-1)^n b_{-n,m}}{1+\delta_{n0}} = g_{n,m}$ ($n = 0, 1, 2\ldots$), from Eqs. (42), (43), (45) and (46), it can be shown that the linear equations for $f_{2n,m}$, $f_{2n+1,m}$, $g_{2n,m}$ and $g_{2n+1,m}$ ($n = 0, 1, 2\ldots$) are completely independent. The linear equations for $f_{2n,m}$ and $g_{2n+1,m}$ are singular at one of the natural frequencies of the channel, but those for $f_{2n+1,m}$ and $g_{2n,m}$ are always bounded. From Eq. (66), $|M_x|$ is in fact related to $g_{2n+1,m}$, and $|M_y|$ is related to $f_{2n+1,m}$. Thus, the behaviours of $|M_x|$ and $|M_y|$ near those natural frequencies reflect the nature of these equations.

4.3. Two different ice sheets separated by a circular crack

We may first consider the case when $h_2 = 0$, or wave diffraction by a circular polynya in an ice-covered channel. In such a case, $K_2(\alpha,\omega)$ in Eq. (35) becomes

$$K_2(\alpha,\omega) = \alpha\tanh\alpha H - \frac{\omega^2}{g}. \tag{75}$$

The summation of m in Eq. (33) is from 0 to $+\infty$, where κ_0 is the purely positive real root of Eq. (75), and κ_m ($m = 1,2,3,\ldots$) are an infinite number of purely negative imaginary roots. The wave elevation in the polynya along x-axis and its comparison with that in an unbounded ocean (Ren et al., 2018) is given in Fig. 12. The physical parameters adopted in Fig. 12 are the same as Fig. 2 in Ren et al.

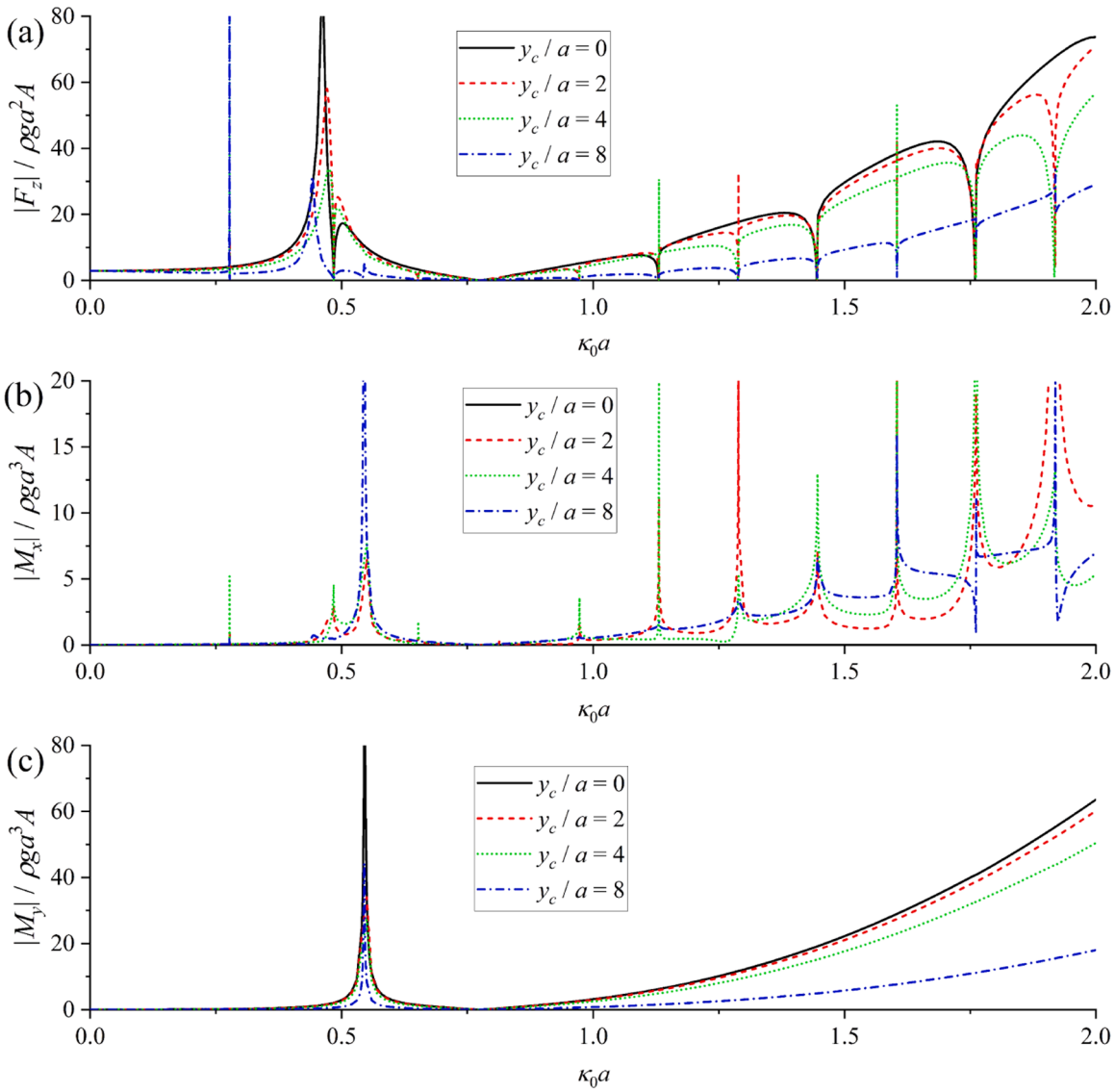

Fig. 11. Force and moment on the inner ice sheet (clamped – clamped on channel wall, $b/a = 10, H/a = 5$, $h_1/a = h_2/a = 0.1$, $y_c/a = 0$). (a) F_z; (b) M_x; (c) M_y.

(2018), and the term $i\omega A$ in Eq. (10) is revised as $-iAg\kappa_0 \tanh\kappa_0 H/\omega$ to be consistent with the ϕ_I in their work. Similar to Fig. 2, with the increases of b/a, the results in channel gradually tend to those in unbounded ocean.

Fig. 13 gives the results of wave transmission and reflection coefficients defined in Eq. (73). With the decrease of h_2/a, the curves of U^T and U^R become more and more oscillatory. This may be related to the resonance of the fluid motion in the inner domain Ω_2. For liquid sloshing in a circular cylindrical container, the natural frequencies may be obtained as (Faltinsen and Timokha, 2009)

$$\omega_{n,m} = \sqrt{k_{n,m} g \tanh k_{n,m} H},\ n = 0,\ 1,\ 2\ldots,\ m = 1,\ 2,\ 3\ldots \tag{76}$$

where $k_{n,m}$ denotes the m-th root of $\mathscr{J}_n'(k_{n,m}a) = 0$. In Fig. 13, the range $0 \le \kappa_0 a \le 2$ corresponds to $0 \le \omega\sqrt{a/g} \le 32.5862$. Within this range, a large number of $\omega_{n,m}$ calculated from Eq. (76) can be found and they are close to each other. Although the current polynya problem is not the same as the sloshing problem in a container, these values of $\omega_{n,m}$ may still be used as a reference. Near one of the frequencies, the fluid motion may change rapidly. Correspondingly, U^R and U^T become highly oscillatory against $\kappa_0 a$. We may take $n = 0$ and $m = 10$ in Eq. (76) as an example, which corresponds to $\kappa_0 a = 0.7714$. We plot four wave profiles in Fig. 14 at $\kappa_0 a = 0.769$, 0.770, 0.771 and 0.772, which is near 0.7714. A very large free surface elevation in the polynya can be observed at these frequencies. Also, a slight change in $\kappa_0 a$ can lead to a significant change in the wave profile. This is closely related to the rapid changes observed in Fig. 13. A local close-up near $\kappa_0 a = 0.7714$ is also given in Fig. 13 (b).

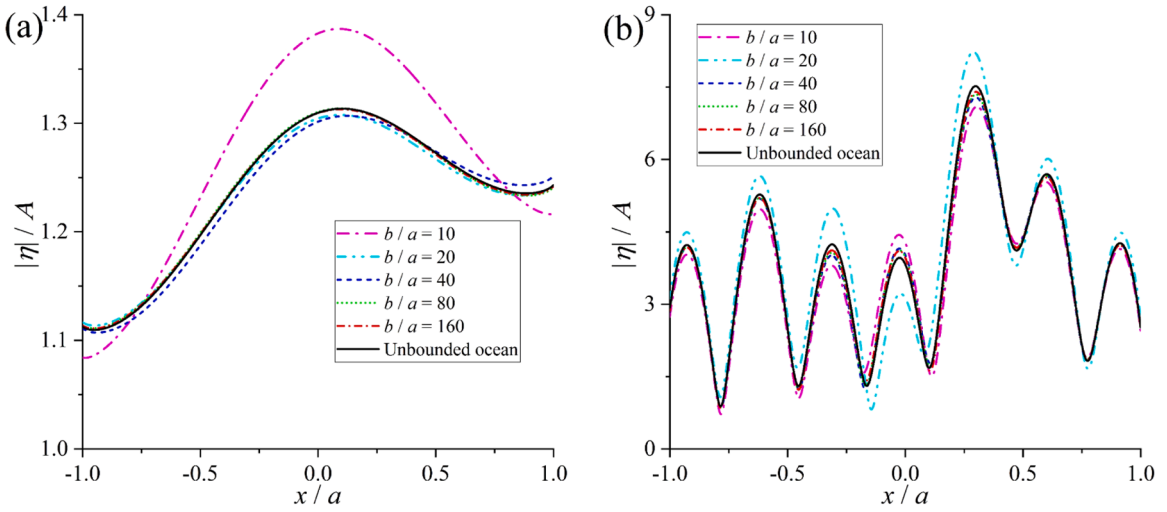

Fig. 12. Wave elevation along x-axis (clamped – clamped on channel walls, $H/a = 2$, $h_1/a = 0.02$, $h_2/a = 0$, $y_c/a = 0$). (a) $\kappa_0 a = 2$; (b) $\kappa_0 a = 4$.

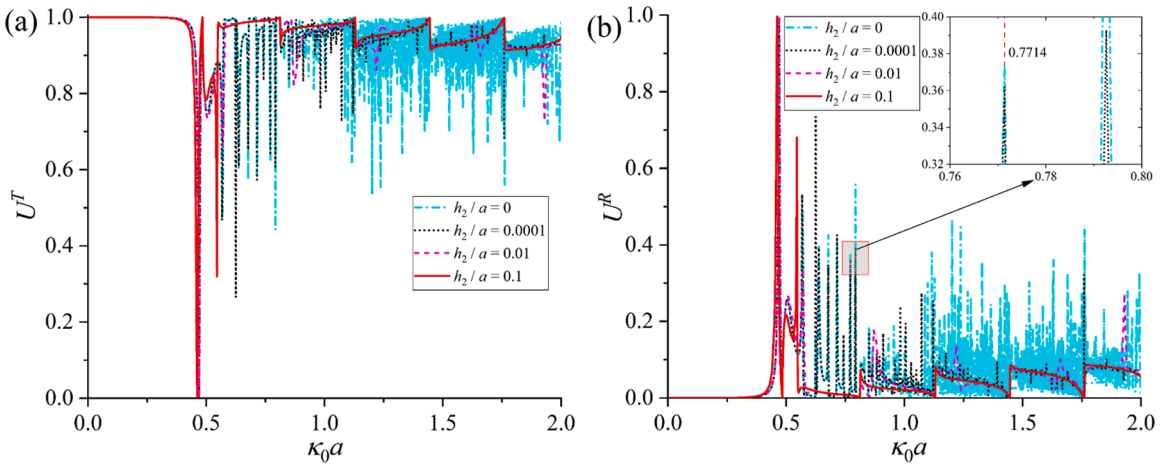

Fig. 13. The wave transmission and reflection coefficients at infinity (clamped – clamped on channel walls, $b/a = 10$, $H/a = 5$, $h_1/a = 0.1$, $y_c/a = 0$) (a) U^T; (b) U^R.

Next, the hydrodynamic forces on the inner ice sheet at different thickness h_1 of the outer ice sheet are considered, the numerical results are given in Fig. 15. When $h_1 = 0$, the problem becomes an elastic disc floating on the free surface channel. It should be noted that $|F_z|$ and $|M_y|$ are nondimensionalized as $|F_z|/\left[\rho g a^2 A\left(\frac{\omega^2 a}{g}\right)\right]$ and $|M_y|/\left[\rho g a^3 A\left(\frac{\omega^2 a}{g}\right)\right]$ respectively. The reason for $\frac{\omega^2 a}{g}$ being used here is because at the same $\kappa_0 a$, ω can be very different at different h_1/a. Normalisation through $\omega^2 a/g$ can help the results to have a similar magnitude. From the figure, it can be seen that when $\frac{\kappa_0 b}{\pi}$ is small, $|F_z|$ and $|M_y|$ in these four cases are nearly the same, which means that the nondimensionalized force and moment on the inner ice sheet at lower frequency region are not sensitive to h_1. This is mainly due to the fact at small $\frac{\kappa_0 b}{\pi}$, the boundary condition on the ice sheet at different thicknesses is all close to that of a rigid plate. When $\frac{\kappa_0 b}{\pi}$ is near one of the natural frequencies of the channel, rapid changes can always be observed on $|F_z|$. Here, as $h_1/a \to 0$, it can be clearly seen that the natural frequencies of the channel gradually tend to those corresponding to the free surface at $\frac{\kappa_0 b}{\pi} = j$ ($j = 1,2,3\ldots$). When $\frac{\kappa_0 b}{\pi}$ is near one of the undamped motion natural frequencies of the channel, a peak can be observed on the curves of $|F_z|$ and $|M_y|$. Typically, from the curves of $h_1/a = 0.1$, 0.05 and 0.02, peaks can be observed at $\frac{\kappa_0 b}{\pi} = 1.4715$, 2.2428 and 3.4635 for $|F_z|$, and at $\frac{\kappa_0 b}{\pi} = 1.7383$, 2.5468 and 4.1224 for $|M_y|$, which indicated that the values of the undamped motion natural frequencies are sensitive to h_1/a. Moreover, as h_1/a decreases, the peak value at each motion natural frequency decreases, and it becomes almost invisible when $h_1/a = 0$.

The strain of the ice sheet is an important parameter related to the fracture of the ice sheet. According to Fung (1977), the principal strains of the inner ice sheet are the eigenvalues of the strain tensor matrix, or

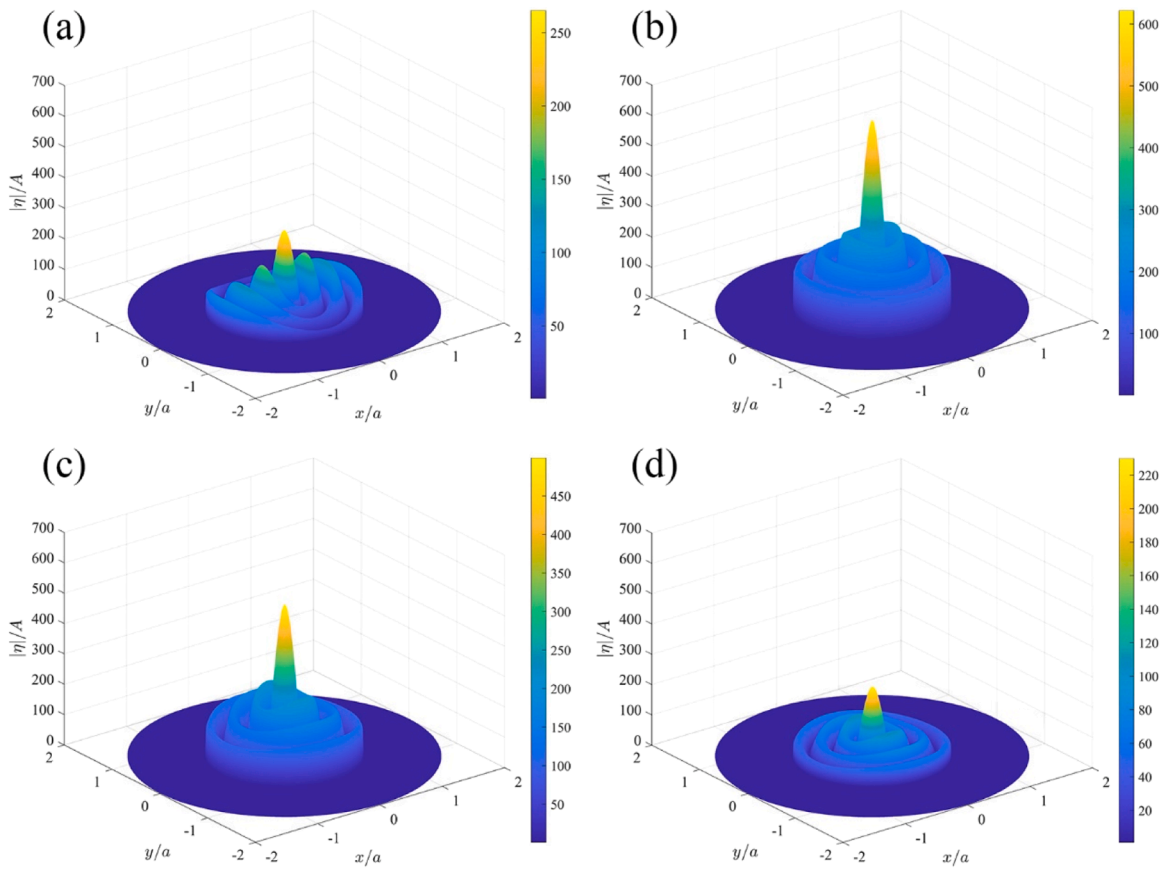

Fig. 14. The modulus of the wave elevation (clamped – clamped on channel walls, $b/a = 10$, $H/a = 5$, $h_1/a = 0.1$, $h_2/a = 0$, $y_c/a = 0$). (a) $\kappa_0 a = 0.769$; (b) $\kappa_0 a = 0.770$; (c) $\kappa_0 a = 0.771$; (d) $\kappa_0 a = 0.772$.

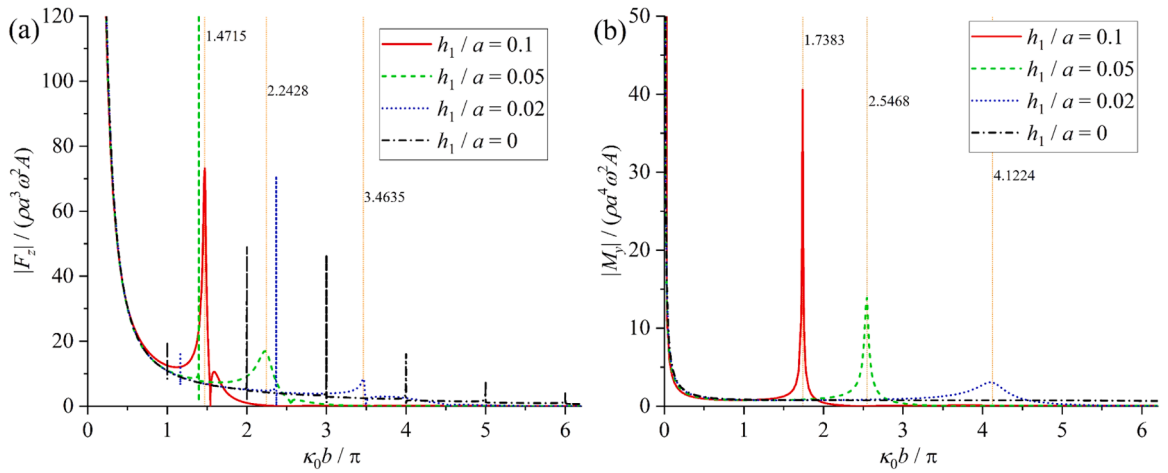

Fig. 15. Force and moment on the inner ice sheet at different thicknesses of the outer ice sheet (clamped – clamped on channel wall, $b/a = 10$, $H/a = 5$, $h_2/a = 0.1$, $y_c/a = 0$). (a) F_z; (b) M_x.

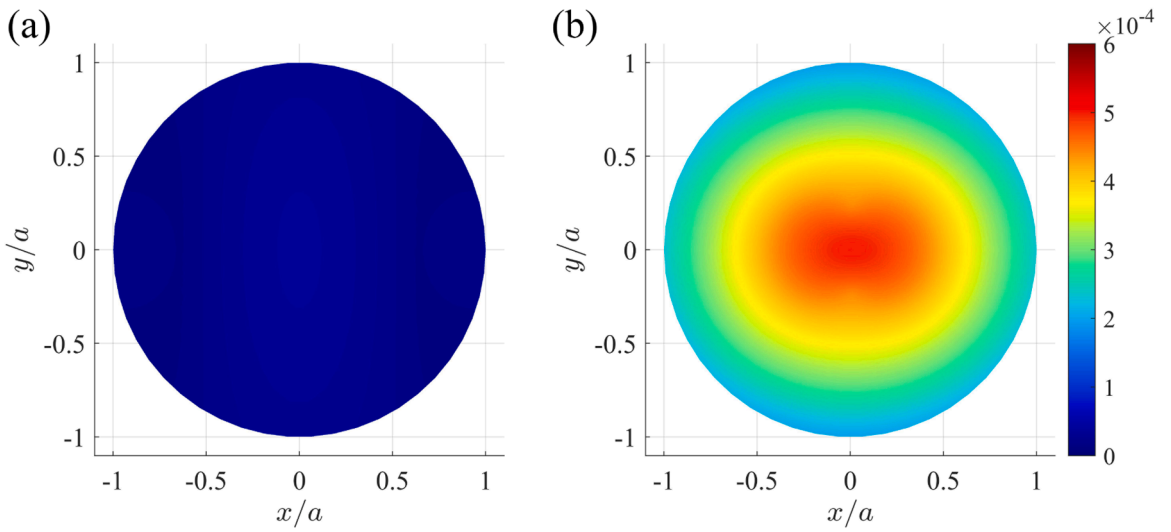

Fig. 16. Distribution of the maximum principal strain $\epsilon_{max}g/\left(\omega^2 A\right)$ in the inner ice sheet at $\kappa_0 b/\pi = 1.4715$. (clamped – clamped on channel wall, $b/a = 10, H/a = 5$, $h_2/a = 0.1$, $y_c/a = 0$). (a) $h_1/a = 0$; (b) $h_1/a = 0.1$.

$$\epsilon = \frac{h_i}{2}\begin{bmatrix}\epsilon_{rr} & \epsilon_{r\theta}\\ \epsilon_{r\theta} & \epsilon_{\theta\theta}\end{bmatrix} = \frac{h_2}{2}\begin{bmatrix}\dfrac{\partial^2 W}{\partial r^2} & \dfrac{1}{r}\dfrac{\partial^2 W}{\partial r\partial\theta} - \dfrac{1}{r^2}\dfrac{\partial W}{\partial\theta}\\ \dfrac{1}{r}\dfrac{\partial^2 W}{\partial r\partial\theta} - \dfrac{1}{r^2}\dfrac{\partial W}{\partial\theta} & \dfrac{1}{r}\dfrac{\partial W}{\partial r} + \dfrac{1}{r^2}\dfrac{\partial^2 W}{\partial\theta^2}\end{bmatrix}, \tag{77}$$

where

$$W(r,\theta,t) = Re\left\{\eta^{(2)}(r,\theta)e^{i\omega t}\right\} = Re\left\{\eta^{(2)}(r,\theta)\right\}\cos\omega t - \mathrm{Im}\left\{\eta^{(2)}(r,\theta)\right\}\sin\omega t, \tag{78}$$

From Eq. (77), the eigenvalues of ϵ are obtained as

$$\varsigma_{1,2} = \frac{h_i}{4}\left[\left(\frac{\partial^2 W}{\partial r^2} + \frac{1}{r}\frac{\partial W}{\partial r} + \frac{1}{r^2}\frac{\partial^2 W}{\partial\theta^2}\right) \pm \sqrt{\left(\frac{\partial^2 W}{\partial r^2} - \frac{1}{r}\frac{\partial W}{\partial r} - \frac{1}{r^2}\frac{\partial^2 W}{\partial\theta^2}\right)^2 + 4\left(\frac{1}{r}\frac{\partial^2 W}{\partial r\partial\theta} - \frac{1}{r^2}\frac{\partial W}{\partial\theta}\right)^2}\right]. \tag{79}$$

Substituting Eq. (78) into Eq. (79) and letting ωt varies from 0 to 2π, the maximum principal strain ϵ_{max} then can be found. Figs. 8 and 13 indicate that the forces and deflection may be quite large near one of the natural frequencies corresponding to the motion of the inner ice sheet. Here, we may make a comparison of the maximum principal strain in the inner sheet with and without the external ice sheet at $\frac{\kappa_0 b}{\pi} = 1.4715$, which is near the natural frequency. ϵ_{max} is presented in Fig. 14, which is nondimensionalized similarly to that in Fig. 13. It can be observed that $\epsilon_{max}g/\left(\omega^2 A\right)$ is much more significant when there is an external ice sheet, which means the inner ice sheet is much more probably to be broken in such a case.

Fig. 16

5. Conclusion

The wave interaction with a circular crack of an ice-cover in a channel has been investigated analytically in this paper. The fluid domain is divided into two parts by the vertical surface extended from the crack. The diffraction potential in the outer domain Ω_1 is constructed through a source distribution formula by using the Green function, and the velocity potential in the inner domain Ω_2 is constructed by adopting the vertical mode expansion and Fourier series expansion. The present method is not just limited to the crack problem, and is applicable to a variety of different problems. The numerical procedure has been verified through the comparison with the results of wave diffraction by a circular crack (Li et al., 2018) and by a polynya (Ren et al., 2018) in the unbounded ocean.

In the paper, the distribution of the roots of the dispersion equation for an ice-cover channel is established. For wave number κ_0 in the unbounded ocean, it is found that all the roots k_j of the dispersion relations $\mathscr{T}_S(k,\omega) = 0$ and $\mathscr{T}_A(k,\omega) = 0$ are located in the range $0 < k < \kappa_0$. When $k \in \left(\lambda_{2j+2}, \lambda_{2j}\right)$, there will be only one root k_{2j} of $\mathscr{T}_S(k,\omega) = 0$, and when $k \in \left(\lambda_{2j+1}, \lambda_{2j-1}\right)$, there will be only one root k_{2j+1} of $\mathscr{T}_A(k,\omega) = 0$, where $\lambda_j = \sqrt{\kappa_0^2 - j^2\pi^2/4b^2}$,. For a finite value of $j < \frac{2b\kappa_0}{\pi}$, all the roots k_j will tend to be κ_0 as $b \to +\infty$. When the thickness of the ice sheet tends to zero, it has been shown that the results tend to those corresponding to the free surface problem.

When $\kappa_0 a$ is near one of the natural frequencies of the channel, sudden changes can be observed in the vertical force $|F_z|$ on the inner ice sheet, as well as in the moment $|M_x|$ if the cylinder is at off-centre position. By contrast, the moment $|M_y|$ varies smoothly. This is

similar to what has been observed from the forces on the vertical cylinder in an ice-covered channel by Yang et al. (2022). For $h_1/a \neq 0$, when $\kappa_0 a$ is near one of the undamped motion natural frequencies of the inner ice sheet, a peak can be observed on $|F_z|$ or $|M_y|$. The values of the motion natural frequencies are not sensitive to the channel width b/a but are very sensitive to outer ice thickness h_1/a. Furthermore, the peak values of $|F_z|$ and $|M_y|$ at these undamped motion natural frequencies gradually decrease as h_1/a decreases and become virtually invisible when $h_1/a = 0$. When $\kappa_0 a$ is near one of the undamped motion natural frequencies, the wave reflection coefficient U^R may tend to 1 and be larger than the transmission coefficient U^T. When the inner ice thickness $h_2/a \to 0$, highly oscillatory behaviours of U^T and U^R have been observed. This may be related to resonance of fluid motion in polynya, similar to liquid sloshing in a circular cylindrical container.

CRediT authorship contribution statement

Y.F. Yang: Writing – original draft, Validation, Software, Methodology, Data curation. **G.X. Wu:** Writing – review & editing, Supervision, Project administration, Methodology, Funding acquisition, Conceptualization. **K. Ren:** Writing – review & editing, Funding acquisition, Formal analysis, Data curation.

Declaration of competing interest

The authors declare that they have no known competing financial interests or personal relationships that could have appeared to influence the work reported in this paper.

Data availability

Data will be made available on request.

Acknowledgements

The third author acknowledges the support of UCL-SJTU Strategic Partner Funds.

Appendix. A. Green function for a channel fully covered by a perfect ice sheet

We may introduce the Green function of a channel fully covered by an ice sheet here. From Yang et al. (2022), the Green function can be written in the following neater and equivalent way,

$$\begin{aligned} G(x,y,z;x_0,y_0,z_0) &= \mathrm{i}\pi \sum_{m=-2}^{+\infty} \frac{\psi_m(z)\psi_m(z_0)}{Q_m} \times \mathscr{H}_0^{(2)}(\kappa_m R) \\ &+ \sum_{m=-2}^{+\infty} \frac{2\psi_m(z)\psi_m(z_0)}{Q_m} \times \int_0^{+\infty} \left[\frac{\cos\sigma_m y \cos\sigma_m y_0}{\sigma_m \sin\sigma_m b} - \mathrm{i} \frac{\sin\sigma_m y \sin\sigma_m y_0}{\sigma_m \cos\sigma_m b} \right] e^{-\mathrm{i}\sigma_m b} \cos k(x-x_0) dk \\ &+ \sum_{m=-2}^{+\infty} \sum_{m'=-2}^{+\infty} \frac{4\psi_{m'}(z)\psi_m(z_0)}{Q_{m'}Q_m} \int_\ell I_{m'}(k)\, I_m(k) \left[\begin{array}{l} \dfrac{\cos\sigma_{m'} y \cos\sigma_m y_0}{\mathscr{T}_S(k,\omega)\sin\sigma_{m'} b \sin\sigma_m b} \\ + \dfrac{\sin\sigma_{m'} y \sin\sigma_m y_0}{\mathscr{T}_A(k,\omega)\cos\sigma_{m'} b \cos\sigma_m b} \end{array} \right] \cos k(x-x_0) dk. \end{aligned} \tag{A1}$$

where

$$\psi_m(z) = \frac{\cosh\kappa_m(z+H)}{\cosh\kappa_m H}, \tag{A2}$$

$$Q_m = \frac{2\kappa_m H + \sinh 2\kappa_m H}{4\kappa_m \cosh^2 \kappa_m H} + \frac{2L_1}{\rho\omega^2}\kappa_m^4 \tanh^2 \kappa_m H. \tag{A3}$$

$$I_m(k) = \zeta_m(k) \times \frac{\kappa_m \tanh\kappa_m H}{\sigma_m}, \tag{A4}$$

$$\left. \begin{aligned} \mathscr{T}_S(k,\omega) &= -2 \sum_{m=-2}^{+\infty} \frac{\kappa_m^2 \tanh^2 \kappa_m H}{Q_m \sigma_m} \times \frac{\zeta_m^2(k)}{\tan\sigma_m b} \\ \mathscr{T}_A(k,\omega) &= 2 \sum_{m=-2}^{+\infty} \frac{\kappa_m^2 \tanh^2 \kappa_m H}{Q_m \sigma_m} \times \zeta_m^2(k) \tan\sigma_m b \end{aligned} \right\}, \tag{A5a, b}$$

with

$$\zeta_m(k) = \begin{cases} 1 & \text{Clamped} - \text{Clamped} \\ \sigma_m^2(k) + \nu_1 k^2 & \text{Free} - \text{Free} \end{cases}, \tag{A6}$$

and $\sigma_m(k) = -\mathrm{i}\left(k^2 - \kappa_m^2\right)^{1/2}$. In Eq. (A1), (x,y,z) and (x_0,y_0,z_0) denote the field and source points respectively, and R represents the distance between (x,y,z) and (x_0,y_0,z_0). $\mathscr{H}_n^{(2)}$ represents the n-th order Hankel function of the second kind, $\alpha = \kappa_m$ are the roots of $K_1(\alpha, \omega) = 0$, where

$$K_1(\alpha,\omega) = \left(L_1\alpha^4 + \rho g - m_1\omega^2\right)\alpha\sinh\alpha H - \rho\omega^2\cosh\alpha H. \tag{A7}$$

In particular, κ_{-2} and κ_{-1} are two complex roots with negative imaginary parts and $\kappa_{-2} = -\bar{\kappa}_{-1}$, where the over bar indicates complex conjugate, κ_0 is the purely positive real root, κ_m ($m = 1,2,3,\ldots$) are an infinite number of purely negative imaginary roots. It should be noted that $\mathscr{T}_S(k,\omega) = 0$ and $\mathscr{T}_A(k,\omega) = 0$ represent the dispersion equations of the ice-covered channel. The roots of the former correspond to the channel natural frequencies of waves symmetric about $x = 0$, while the roots of the latter to those of waves anti-symmetric about $x = 0$. To satisfy the radiation condition at $x = \pm\infty$, the integration path $\curlywedge$ in Eq. (A1) from $k = 0$ to $k = +\infty$ should pass over all the singularities at $\mathscr{T}_S(k,\omega) = 0$ and $\mathscr{T}_A(k,\omega) = 0$. It should be noted that $\mathscr{T}_S(k,\omega) \times \mathscr{T}_A(k,\omega) = 0$ may have multiple real positive roots. We may denote them as k_j ($j = 0\ldots N_S - 1$) here, with $k_{j+1} < k_j$. k_{2j} are the roots of $\mathscr{T}_S(k,\omega) = 0$, while k_{2j+1} are the roots of $\mathscr{T}_A(k,\omega) = 0$, the graphical representation of these roots can be found in Ren et al. (2020) and Yang et al. (2022). Physically, each k_j is the wavenumber of the j-th longitudinal wave generated by the Green function. In the free surface channel with $h_1 = 0$, $k_j = \sqrt{\kappa_0^2 - \frac{j^2\pi^2}{4b^2}}$ and it corresponds to a unique transverse mode $\cos\frac{j\pi}{2b}(y+b)$. By contrast, for an ice sheet or $h_1 \neq 0$, all the transverse modes here are coupled, or for each wave component k_j at infinity, all the other transverse modes exist, although the mode corresponding to $\frac{j\pi}{2b}$ may still be dominant. We may also notice that there are also singularities in the two integrations of the Green function when the sine or cosine functions in the denominator are equal to zero. However, the residuals of the two integrations at these points cancel each other. Therefore, the Cauchy principal integrations are implied at these singular points.

Appendix. B. The Boundary integral equation of ϕ and $\overline{\phi}$ at infinity

We may apply the Green's second identity to velocity potential ϕ and its complex conjugate $\overline{\phi}$ over the entire fluid boundary S, which gives

$$\oiint_S \left[\phi(x,y,z)\frac{\partial\overline{\phi}(x,y,z)}{\partial n} - \overline{\phi}(x,y,z)\frac{\partial\phi(x,y,z)}{\partial n}\right]dS = 0. \tag{B1}$$

By applying a similar procedure in Yang et al. (2021), only the integrations over the two vertical surface $S_{\pm\infty}$ at far-field and along two lines at $x = \pm\infty$ & $z = 0$ need to be kept, which provides

$$\iint_{S_{+\infty}} \left(\phi\frac{\partial\overline{\phi}}{\partial x} - \overline{\phi}\frac{\partial\phi}{\partial x}\right)dS - \iint_{S_{-\infty}} \left(\phi\frac{\partial\overline{\phi}}{\partial x} - \overline{\phi}\frac{\partial\phi}{\partial x}\right)dS + \frac{L_1}{\rho\omega^2}\int_{-b}^{b}\left(\frac{\partial\overline{\phi}}{\partial z}\frac{\partial}{\partial x}\nabla^2\frac{\partial\phi}{\partial z} - \frac{\partial^2\overline{\phi}}{\partial x\partial z}\nabla^2\frac{\partial\phi}{\partial z} - \frac{\partial\phi}{\partial z}\frac{\partial}{\partial x}\nabla^2\frac{\partial\overline{\phi}}{\partial z} + \frac{\partial^2\phi}{\partial x\partial z}\nabla^2\frac{\partial\overline{\phi}}{\partial z}\right)_{z=0}\Bigg|_{x=-\infty}^{x=+\infty}dy = 0. \tag{B2}$$

Applying the Laplace equation into Eq. (B2), we have

$$\begin{aligned}&\int\int_{S_{+\infty}}\left(\phi\frac{\partial\overline{\phi}}{\partial x} - \overline{\phi}\frac{\partial\phi}{\partial x}\right)dS - \int\int_{S_{-\infty}}\left(\phi\frac{\partial\overline{\phi}}{\partial x} - \overline{\phi}\frac{\partial\phi}{\partial x}\right)dS \\ &+\frac{L_1}{\rho\omega^2}\int_{-b}^{b}\left(\frac{\partial\phi}{\partial z}\frac{\partial^4\overline{\phi}}{\partial x\partial z^3} + \frac{\partial^3\phi}{\partial z^3}\frac{\partial^2\overline{\phi}}{\partial x\partial z} - \frac{\partial\overline{\phi}}{\partial z}\frac{\partial^4\phi}{\partial x\partial z^3} - \frac{\partial^3\overline{\phi}}{\partial z^3}\frac{\partial^2\phi}{\partial x\partial z}\right)_{z=0}\Bigg|_{x=-\infty}^{x=+\infty}dy = 0.\end{aligned} \tag{B3}$$

Define

$$I_{\pm}(x) = \iint_{S_{\pm\infty}}\left(\phi\frac{\partial\overline{\phi}}{\partial x} - \overline{\phi}\frac{\partial\phi}{\partial x}\right)dS + \frac{L_1}{\rho\omega^2}\int_{-b}^{b}\left(\frac{\partial\phi}{\partial z}\frac{\partial^4\overline{\phi}}{\partial x\partial z^3} + \frac{\partial^3\phi}{\partial z^3}\frac{\partial^2\overline{\phi}}{\partial x\partial z} - \frac{\partial\overline{\phi}}{\partial z}\frac{\partial^4\phi}{\partial x\partial z^3} - \frac{\partial^3\overline{\phi}}{\partial z^3}\frac{\partial^2\phi}{\partial x\partial z}\right)_{z=0,x=\pm\infty}dy. \tag{B4}$$

Invoking the inner product in Eq. (22), $I_{\pm}(x)$ can be further expressed as

$$I_{\pm}(x)=\int_{-b}^{b}\left[\left\langle\phi,\frac{\partial\overline{\phi}}{\partial x}\right\rangle-\left\langle\overline{\phi},\frac{\partial\phi}{\partial x}\right\rangle\right]_{x=\pm\infty}dy. \tag{B5}$$

Here, we may consider

$$\begin{aligned}\frac{dI_{\pm}}{dx}=&\int\int_{S_{\pm\infty}}\left(\phi\frac{\partial^2\overline{\phi}}{\partial x^2}-\overline{\phi}\frac{\partial^2\phi}{\partial x^2}\right)dS\\&+\frac{L_1}{\rho\omega^2}\int_{-b}^{b}\left(\frac{\partial\phi}{\partial z}\frac{\partial^5\overline{\phi}}{\partial x^2\partial z^3}+\frac{\partial^3\phi}{\partial z^3}\frac{\partial^3\overline{\phi}}{\partial x^2\partial z}-\frac{\partial\overline{\phi}}{\partial z}\frac{\partial^5\phi}{\partial x^2\partial z^3}-\frac{\partial^3\overline{\phi}}{\partial z^3}\frac{\partial^3\phi}{\partial x^2\partial z}\right)_{z=0,x=\pm\infty}dy.\end{aligned} \tag{B6}$$

Applying the Laplace equation into Eq. (B6), we have

$$\begin{aligned}\frac{dI_{\pm}}{dx}=&\int\int_{S_{\pm\infty}}\left(\overline{\phi}\nabla_{yz}^2\phi-\phi\nabla_{yz}^2\overline{\phi}\right)dS\\&+\frac{L_1}{\rho\omega^2}\int_{-b}^{b}\left(\frac{\partial\phi}{\partial z}\frac{\partial^5\overline{\phi}}{\partial x^2\partial z^3}+\frac{\partial^3\phi}{\partial z^3}\frac{\partial^3\overline{\phi}}{\partial x^2\partial z}-\frac{\partial\overline{\phi}}{\partial z}\frac{\partial^5\phi}{\partial x^2\partial z^3}-\frac{\partial^3\overline{\phi}}{\partial z^3}\frac{\partial^3\phi}{\partial x^2\partial z}\right)_{z=0,x=\pm\infty}dy,\end{aligned} \tag{B7}$$

where ∇_{yz}^2 denotes the Laplace operator on the $O-yz$ plane. By using a similar procedure in Yang et al. (2021) again, we can obtain

$$\frac{dI_{\pm}}{dx}=0, \tag{B8}$$

which suggests that $I_{\pm}$ is independent to x.

References

Abramowitz, M., Stegun, I.A., 1965. Handbook of mathematical functions with formulas, graphs, and mathematical table. US Department of Commerce. National Bureau of Standards Applied Mathematics series, p. 55.

Anon. NASA, 2013. Breakup continues on the wilkins ice shelf, https://earthobservatory.nasa.gov/images/81174/breakup-continues-on-the-wilkins-ice-shelf.

Balmforth, N.J., Craster, R.V., 1999. Ocean waves and ice sheets. J. Fluid Mech. 395, 89–124.

Bennetts, L.G., Williams, T.D., 2010. Wave scattering by ice floes and polynyas of arbitrary shape. J. Fluid Mech. 662, 5–35.

Chung, H., Linton, C.M., 2005. Reflection and transmission of waves across a gap between two semi-infinite elastic plates on water. Quart. J. Mech. Appl. Math. 58, 1–15.

Collins III, C.O., Rogers, W.E., Marchenko, A., Babanin, A.V., 2015. In situ measurements of an energetic wave event in the Arctic marginal ice zone. Geophys. Res. Lett. 42, 1863–1870.

Evans, D.V., Porter, R., 2003. Wave scattering by narrow cracks in ice sheets floating on water of finite depth. J. Fluid Mech. 484, 143.

Ewing, M., Crary, A., 1934. Propagation of elastic waves in ice. Part II. Physics. 5, 181–184.

Faltinsen, O.M., Timokha, A.N., 2009. Sloshing. Cambridge university press Cambridge.

Fox, C., Squire, V.A., 1994. On the oblique reflexion and transmission of ocean waves at shore fast sea ice. Philosophical Transactions of the Royal Society of London. Phys. Eng. Sci. 347, 185–218.

Fung, Y.C., 1977. A first course in continuum mechanics. Englewood Cliffs.

Jansson, P., Näslund, J.O., Rodhe, L., 2007. Ice sheet hydrology-a review.

Khabakhpasheva, T., Shishmarev, K., Korobkin, A., 2019. Large-time response of ice cover to a load moving along a frozen channel. Appl. Ocean Res. 86, 154–165.

Korobkin, A.A., Khabakhpasheva, T.I., Papin, A.A., 2014. Waves propagating along a channel with ice cover. Euro. J. Mech.B/Fluids 47, 166–175.

Lazzara, M.A., Jezek, K.C., Scambos, T.A., MacAyeal, D.R., Van der Veen, C.J., 1999. On the recent calving of icebergs from the ross ice shelf. Polar Geography 23, 201–212.

Li, Z.F., Wu, G.X., Shi, Y.Y., 2018. Wave diffraction by a circular crack in an ice sheet floating on water of finite depth. Phys. Fluids 30, 117103.

Li, Z.F., Wu, G.X., Ren, K., 2020. Wave diffraction by multiple arbitrary shaped cracks in an infinitely extended ice sheet of finite water depth. J. Fluid Mech. 893.

Mandal, S., Law, A.W.K., Shen, H.H., 2018. Wave interactions with circular ice ridge embedded in level ice. Cold. Reg. Sci. Technol. 155, 90–99.

Marchenko, A.V., 1993. Surface wave diffraction at a crack in sheet ice. Fluid Dyn. 28, 230–237.

Meylan, M.H., Squire, V.A., 1996. Response of a circular ice floe to ocean waves. Oceans 101, 8869–8884.

Montiel, F., Bennetts, L.G., Squire, V.A., Bonnefoy, F., Ferrant, P., 2013. Hydroelastic response of floating elastic discs to regular waves. Part 2. Modal analysis. J. Fluid Mech. 723, 629–652.

Porter, R., Evans, D.V., 2006. Scattering of flexural waves by multiple narrow cracks in ice sheets floating on water. Wave Motion. 43, 425–443.

Porter, R., Evans, D.V., 2007. Diffraction of flexural waves by finite straight cracks in an elastic sheet over water. J. Fluids. Struct. 23, 309–327.

Porter, R., 2019. The coupling between ocean waves and rectangular ice sheets. J. Fluids Struct. 84, 171–181.

Ren, K., Wu, G.X., Ji, C.Y., 2018. Wave diffraction and radiation by a vertical circular cylinder standing in a three-dimensional polynya. J. Fluids Struct. 82, 287–307.

Ren, K., Wu, G.X., Li, Z.F., 2020. Hydroelastic waves propagating in an ice-covered channel. J. Fluid Mech. 886.

Ren, K., Wu, G.X., Li, Z.F., 2021. Natural modes of liquid sloshing in a cylindrical container with an elastic cover. J. Sound. Vib. 512, 116390.

Sahoo, T., Yip, T.L., Chwang, A.T., 2001. Scattering of surface waves by a semi-infinite floating elastic plate. Phys. Fluids 13, 3215–3222.

Shi, Y.Y., Li, Z.F., Wu, G.X., 2019. Interaction of wave with multiple wide polynyas. Phys. Fluids 31, 067111.

Shishmarev, K., Khabakhpasheva, T., Korobkin, A., 2016. The response of ice cover to a load moving along a frozen channel. Appl. Ocean Res. 59, 313–326.

Squire, V.A., Dixon, T.W., 2000. An analytic model for wave propagation across a crack in an ice sheet. Internat. J. Offshore Polar Eng. 10.

Squire, V.A., Dugan, J.P., Wadhams, P., Rottier, P.J., Liu, A.K., 1995. Of ocean waves and sea ice. Annu Rev. Fluid. Mech. 27, 115–168.

Sturova, I.V., 1999. Oblique incidence of surface waves on an elastic plate. J. Appl. Mech. Techn. Phys. 40, 604–610.

Timoshenko, S.P., Woinowsky-Krieger, S., 1959. Theory of plates and shells. McGraw-hill.
Wang, C.D., Meylan, M.H., 2004. A higher-order-coupled boundary element and finite element method for the wave forcing of a floating elastic plate. J. Fluids. Struct. 19, 557–572.
Williams, T.D., Squire, V.A., 2002. Wave propagation across an oblique crack in an ice sheet. In: The Twelfth international offshore and polar engineering conference. OnePetro.
Williams, T.D., Squire, V.A., 2006. Scattering of flexural–gravity waves at the boundaries between three floating sheets with applications. J. Fluid Mech. 569, 113–140.
Wu, G.X., 1998a. Wave radiation and diffraction by a submerged sphere in a channel. Q. J. Mech. Appl. Math. 51, 647–666.
Wu, G.X., 1998b. Wavemaking resistance on a submerged sphere in a channel. J. Ship Res. 42, 1–8.
Yang, Y.F., Wu, G.X., Ren, K., 2021. Three-dimensional interaction between uniform current and a submerged horizontal cylinder in an ice-covered channel. J. Fluid Mech. 928, A4.
Yang, Y.F., Wu, G.X., Ren, K., 2022. Hydroelastic wave diffraction by a vertical circular cylinder standing in a channel with an ice cover. J. Fluid Mech. 941, A13.